

Comparison of Scene Contrast Temperature in MWIR and LWIR

by

Shane Jordan

---

Copyright © Shane Jordan 2024

A Thesis Submitted to the Faculty of the

JAMES C. WYANT COLLEGE OF OPTICAL SCIENCES

In Partial Fulfillment of the Requirements

For the Degree of

MASTER OF SCIENCE

In the Graduate College

THE UNIVERSITY OF ARIZONA

2024

THE UNIVERSITY OF ARIZONA  
GRADUATE COLLEGE


As members of the Master's Committee, we certify that we have read the thesis prepared by **Shane Henry Jordan**, titled *Comparison of Scene Contrast Temperature in MWIR and LWIR* and recommend that it be accepted as fulfilling the thesis requirement for the Master's Degree.

  
\_\_\_\_\_  
Professor Ronald G. Driggers

Date: 4/3/24

  
\_\_\_\_\_  
Professor David Brady

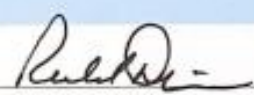
Date: 4/3/24

  
\_\_\_\_\_  
Dr. Orges Furxhi

Date: 04/03/2024

Final approval and acceptance of this thesis is contingent upon the candidate's submission of the final copies of the thesis to the Graduate College.

I hereby certify that I have read this thesis prepared under my direction and recommend that it be accepted as fulfilling the Master's requirement.

  
\_\_\_\_\_  
Professor Ronald G. Driggers  
Master's Thesis Committee Chair  
Wyant College of Optical Sciences

Date: 4/3/24

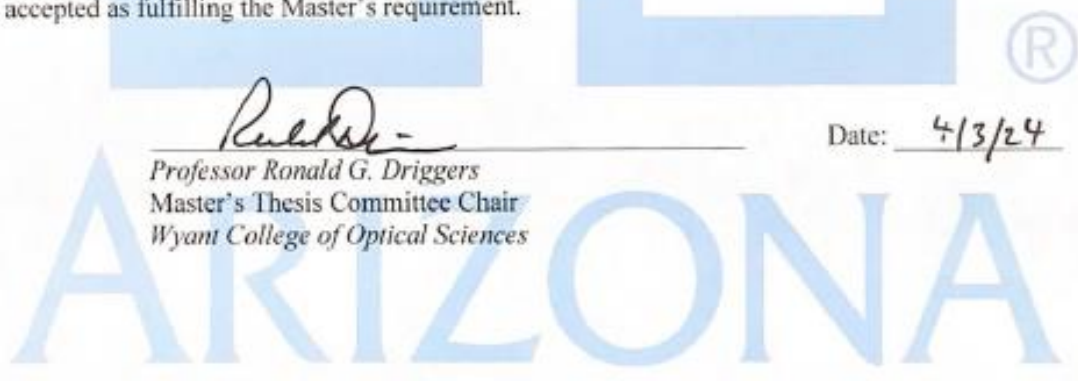


## TABLE OF CONTENTS

LIST OF FIGURES .....	5
LIST OF TABLES .....	7
ABSTRACT .....	8
Chapter 1 Introduction .....	9
Chapter 2 Background .....	11
2.1 Radiometry and Planck’s Curve.....	11
2.2 Infrared Imaging.....	16
2.3 What is Scene Contrast Temperature? .....	21
2.4 Importance of SCT.....	24
2.5 What influences SCT?.....	28
2.6 Previous Research in SCT.....	29
Chapter 3 Theoretical Calculations.....	33
3.1 Contrast Calculations .....	33
3.2 Pilotage Performance .....	36
Chapter 4 Experimental Description.....	39
4.1 Goal .....	39
4.2 Sensors .....	39
4.3 Calibration.....	40
4.4 Conditions .....	42
4.5 Sources of Error .....	43
Chapter 5 Experimental Results.....	47
5.1 Diurnal .....	47
5.2 Rural.....	50
5.3 Urban.....	52

5.4 Humid Environment.....	55
5.5 Precipitation .....	56
Chapter 6 Discussion .....	60
Chapter 7 Conclusions .....	66
REFERENCES .....	67

## LIST OF FIGURES

Figure 2.1: The electromagnetic spectrum [1]. Public Domain.....	11
Figure 2.2: Planck's and Wien's Law (dotted line represents Wien's law).....	13
Figure 2.3: Atmospheric transmission spectrum [1]. Public Domain.....	14
Figure 2.4: Solar Radiance Curve.....	15
Figure 2.5: 300K Blackbody Radiance Curve.....	15
Figure 2.6: Progression of information through an EO/IR system.....	17
Figure 2.7: Higher-resolution image (left) and lower-resolution image (right).....	17
Figure 2.8: Higher SNR image (left), lower SNR image (right).....	19
Figure 2.9: Images depicting effects of variation in SCT and $\sigma T$ (low SCT right, high SCT left, low $\sigma T$ top, high $\sigma T$ bottom).....	24
Figure 2.10: Typical Pilotage Sensor Performance Curve as a function of SCT. Example images correspond to dotted lines.....	26
Figure 2.11: Low SCT image (left) and the high SCT image (right).....	28
Figure 3.1: Planck's curve for emittance from a 300K equivalent blackbody in $W/cm^2$ and $p/s-cm^2$ .....	35
Figure 3.2: LWIR/MWIR TTP vs SCT in a pilotage context ( $C_{tgt}=1$ ) for different F-numbers...	37
Figure 3.3: LWIR pilotage sensor TTP vs SCT for various NETD values.....	38
Figure 4.1: Linear relationship of equivalent blackbody temperature to gray level.....	41
Figure 4.2: Resulting histograms from analysis of a single scene comparison between LWIR (left) and MWIR (right).....	42
Figure 4.3: Noise depiction (MWIR left, LWIR right).....	44
Figure 4.4: Percentage of dynamic range vs contrast temperature, SCT=10K.....	45
Figure 4.5: Percentage of dynamic range vs contrast temperature, SCT=50K.....	46
Figure 5.1: Sample diurnal imagery (MWIR top, LWIR bottom; daytime left, nighttime right), boxes show area analyzed.....	48
Figure 5.2: MWIR vs LWIR scene contrast over a 24-hour diurnal cycle.....	49
Figure 5.3: Diurnal FOM (Eq. 8) as function of time.....	50
Figure 5.4: Sample rural imagery (MWIR top, LWIR bottom; daytime left, nighttime right), boxes indicate area analyzed.....	51
Figure 5.5: Rural scene $\sigma T$ distribution for daytime and nighttime.....	52
Figure 5.6: Sample urban imagery (MWIR top, LWIR bottom; daytime left, nighttime right), boxes indicate area analyzed.....	53
Figure 5.7: Urban scene $\sigma T$ distribution for daytime, nighttime, and daytime with clouds.....	54

Figure 5.8: Sample humid urban imagery (MWIR left, LWIR right). .....	55
Figure 5.9: Humid rural scene $\sigma T$ distribution .....	56
Figure 5.10: LWIR vs MWIR $\sigma T$ during rainfall. ....	57
Figure 5.11: LWIR vs MWIR $\sigma T$ over time during and after rainfall. ....	58
Figure 5.12: FOM (Eq. 8) as function of time during and after rainfall. ....	59
Figure 6.1: Low NETD Pilotage Sensor TTP vs time over multiple days (using precipitation data) for LWIR/MWIR .....	63
Figure 6.2 : Medium NETD Pilotage Sensor TTP vs time over multiple days (using precipitation data) for LWIR/MWIR .....	64
Figure 6.3: High NETD Pilotage Sensor TTP vs time over multiple days (using precipitation data) for LWIR/MWIR .....	64

**LIST OF TABLES**

Table 2.1: Radiometry units.....	12
Table 3.1: Comparison of radiometric units and contrast calculations.....	34
Table 3.2: Sample pilotage system specifications .....	36
Table 4.1: System Information .....	40
Table 5.1: FOM (Eq. 8) results for rural scenes. ....	52
Table 5.2: FOM (Eq. 8) results for urban scenes.....	54
Table 5.3: FOM (Eq. 8) results for humid scenes.....	56
Table 6.1: Average FOM (Eq. 8) calculations for each set of individual scene data .....	60

## ABSTRACT

*The contents of this manuscript are a modification of the following publication:*

Shane Jordan, Ronald Driggers, Orges Furxhi, Patrick Leslie, Col Cavanaugh, Kyle Renshaw, Eddie Jacobs, "Comparison of scene contrast temperature in mid-wave infrared and long-wave infrared," *Opt. Eng.* 62(11) 113107 (27 November 2023)

Infrared imagers are used for many applications, these include target acquisition (both target search and target identification), threat warning, aircraft detection, and pilotage. Scene contrast temperature (SCT) describes the radiometric temperature associated with the dynamic range of an imager and is an important factor in the performance of all of these applications; it can be just as important in the performance of the sensor in an application. A few examples are: 1) a high scene contrast with clutter can increase the difficulty of target search, 2) a high scene contrast with image-based navigation can enhance the performance of location estimation, and 3) high scene contrast with mobility sensors can enhance the performance of a rotorcraft pilotage system.

SCT is influenced by the range of radiance in the scene; the temperature and emissivity of each object in a scene determines this range. The range of radiance in a scene is dependent on the band in which the imager is sensitive because blackbody emission and emissivity both vary with spectrum. This work investigates the differences in SCT between the mid-wave infrared (MWIR) and long-wave infrared (LWIR) spectra in different environments and conditions. In daytime conditions, SCT is found to be greater in MWIR, and SCT is found to be higher in LWIR in nighttime conditions. Cloudy conditions during the daytime decrease SCT regardless of band, and rainy conditions are found to dramatically decrease SCT regardless of band. The effects of these spectral differences are extrapolated to imaging performance in a pilotage scenario.



## Chapter 1 Introduction

For any application that an infrared imaging system is used for, both the resolution and the sensitivity of these systems dictate their performance. The resolution of the system is determined by the total blur in the system; low resolution is manifested as a loss of contrast in higher spatial frequency components of an image. Sensitivity is determined by the noise in a system; high sensitivity systems can discern very small differences in radiance from different parts of the scene, while these small differences get “washed out” by random noise in low sensitivity systems. The capacity of an imager to efficiently convey information to the user is a combination of resolution and sensitivity.

The task difficulty for an infrared imager is determined by the scene. Scenes with small variations in radiance necessitate high sensitivity imagers. Scenes with small features, such as a scene which is very far away, necessitate high resolution imagers. The size of the features in the scene are entirely dependent on the application, but the variation in radiance between those features, the scene contrast, is partially dependent on the wavelengths at which the imager is sensitive; blackbody emission and emissivity both vary with wavelength.

For scenes with high scene contrast, dynamic range is set such that small variations, such as noise, in measured radiance result in small variations in display luminance. This results in a high-quality image as these scenes have large variations in emitted signal. For scenes with low scene contrast, when the scene dynamic range is stretched across the display dynamic range, small variations in measured radiance and noise become apparent. A very sensitive imager is able to stretch this dynamic range to discriminate very small variations in emitted signal from the scene before noise begins to drown out these variations.

Mid-wave infrared (MWIR) and long-wave infrared (LWIR) imagers are capable of sensing light emitted by objects that are at temperatures corresponding to earth conditions ( $\sim 300\text{K}$ ). The subject of this study is Scene Contrast Temperature (SCT), which is a measure of the dynamic range of a scene in terms of equivalent blackbody temperature for these emissive infrared wavelength bands. These thermal sensors need to be sensitive enough to pick up very small variations in scene radiance due to slight differences in temperature throughout the scene. Since these variations differ between bands, this study investigates the extent of these differences. Additionally, the propagation of these differences to the ultimate performance of an imager is investigated.

## Chapter 2 Background

### 2.1 Radiometry and Planck's Curve

Light exists on a spectrum of electromagnetic radiation, which travels as waves at different wavelengths. This spectrum includes radio waves, microwaves, and infrared light at the longer end of the spectrum, and ultra-violet, x-rays, and gamma rays at the shorter end of the spectrum. Figure 2.1 shows the electromagnetic spectrum over a range of wavelengths from meters down to femtometers.

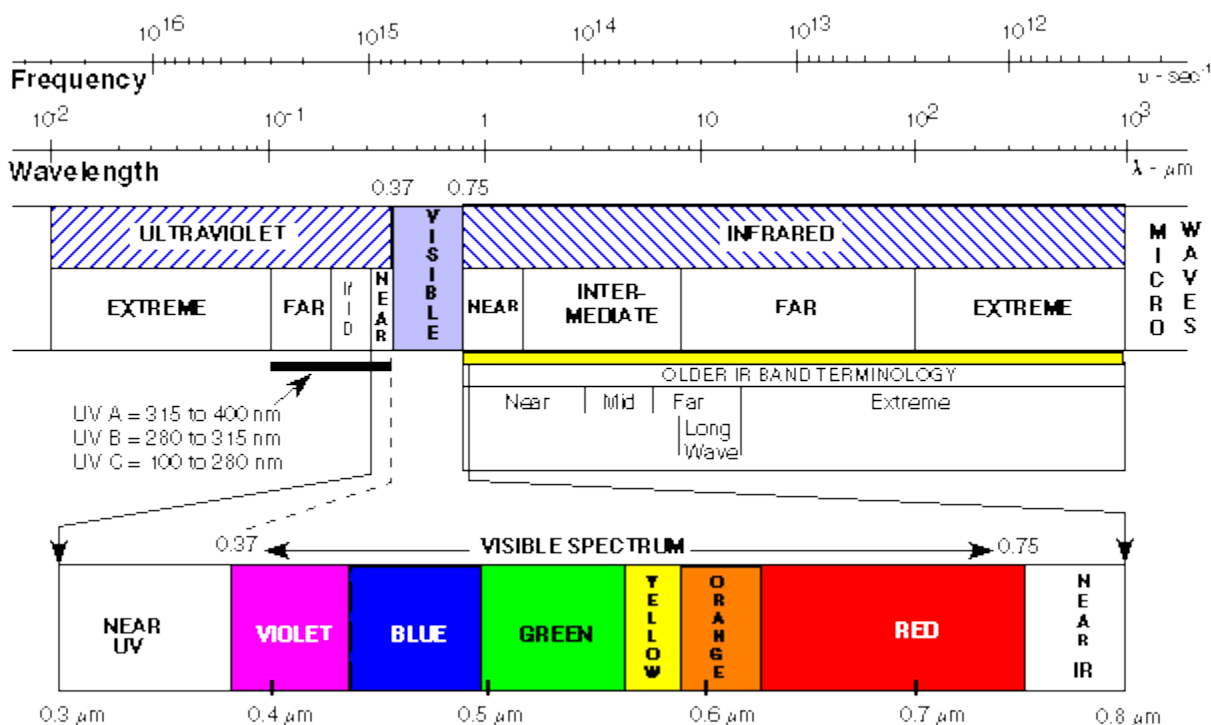


Figure 2.1: The electromagnetic spectrum [1]. Public Domain.

Light travels in waves but can also be represented as photons. Photons are individualized packets of electromagnetic energy, with energy dependent on the wavelength of the photon. The energy in a singular photon is as follows:

$$E = \frac{hc}{\lambda} [J] \quad (1)$$

Where  $h$  is Planck's constant ( $6.626 \times 10^{-34}$  J-s),  $c$  is the speed of light in a vacuum ( $3 \times 10^8$  m/s), and  $\lambda$  is the wavelength of the photon. Electromagnetic flux is associated with the total photon flux and is primarily measured in Watts (J/s) over all spectra, where shorter, more energetic wavelengths contain more Joules per photon. In order to describe sources of light, it is first important to describe the radiometry and units associated with the spread of light. Table 1 reports the primary units which describe sources and terminals of light.

Table 2.1: Radiometry units

<b>Name</b>	<b>Unit</b>	<b>Explanation</b>
<b>Watt</b>	$\frac{J}{s}$	Flux – amount of energy per unit time
<b>Intensity</b>	$\frac{W}{sr}$	Flux per steradian exiting a source
<b>Exitance</b>	$\frac{W}{m^2}$	Total flux exiting the surface area of a source
<b>Emittance</b>	$\frac{W}{m^2}$	Flux emitted from the surface area of a source
<b>Irradiance</b>	$\frac{W}{m^2}$	Total flux incident on a terminal
<b>Radiance</b>	$\frac{W}{m^2 - sr}$	Flux per steradian per unit area

Electro-optic/infrared (EO/IR) sensors are designed to observe sources of light in the visible and infrared bands. The dominant source of light in the visible and infrared bands is blackbody radiation, the random emission of photons due to thermal energy. All objects emit blackbody radiation in accordance with Planck's law, which governs the radiance of a thermal source as a function of wavelength and temperature. The general form of Planck's Law is as follows:

$$L_{\lambda} = \frac{2h\nu^5}{n^2c^3} \frac{1}{e^{\frac{h\nu}{k_B T}} - 1} \left( \frac{W}{\text{cm}^2 \text{sr} \mu\text{m}} \right) \quad (2)$$

Where  $n$  is the refractive index,  $\lambda$  is the wavelength in microns,  $\nu$  is the frequency of the light in Hz,  $k$  is the Boltzmann constant ( $1.38\text{E-}34$  J/K), and  $T$  is the temperature of the object. There are two important attributes of Planck's law: radiance increases monotonically with temperature regardless of wavelength, and the peak emission wavelength decreases as a function of temperature, defined by Wien's law is as follows:

$$\lambda_{peak} = \frac{2898}{T} [\mu\text{m}] \quad (3)$$

Figure 2.2 is a depiction of Wien's law within Planck's law. The wavelength at which the blackbody emission curve peaks at lower and lower wavelengths with increasing temperature.

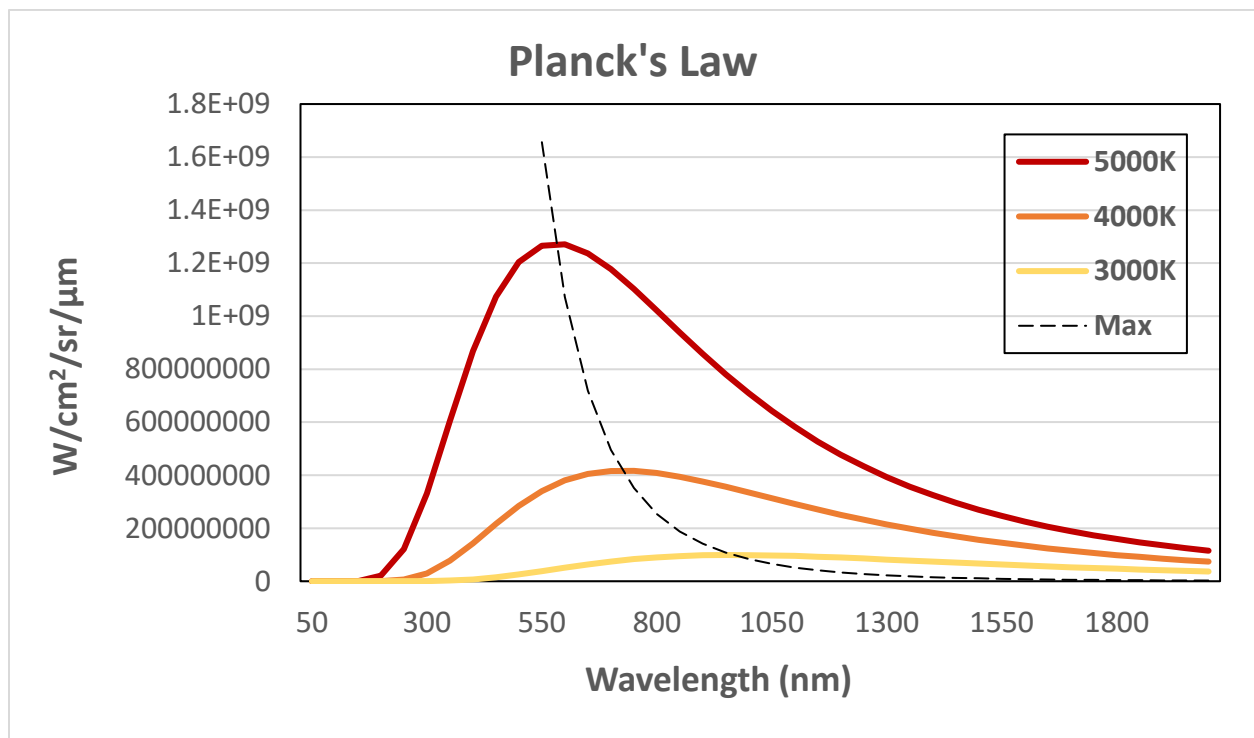


Figure 2.2: Planck's and Wien's Law (dotted line represents Wien's law)

EO/IR sensors sense wavelengths integrated in “bands”. Wavelength bands are usually defined by windows in the atmosphere where emission at a given wavelength can pass through the atmosphere without being absorbed. Figure 2.3 depicts the atmospheric windows – visible (VIS) from 0.4 to 0.7 microns, near-infrared (NIR) from 0.7 to 1.1 microns, shortwave-infrared (SWIR) from 1.1 to 1.7 microns, midwave infrared (MWIR) from 3 to 5 microns, and longwave infrared (LWIR) from 8 to 14 microns.

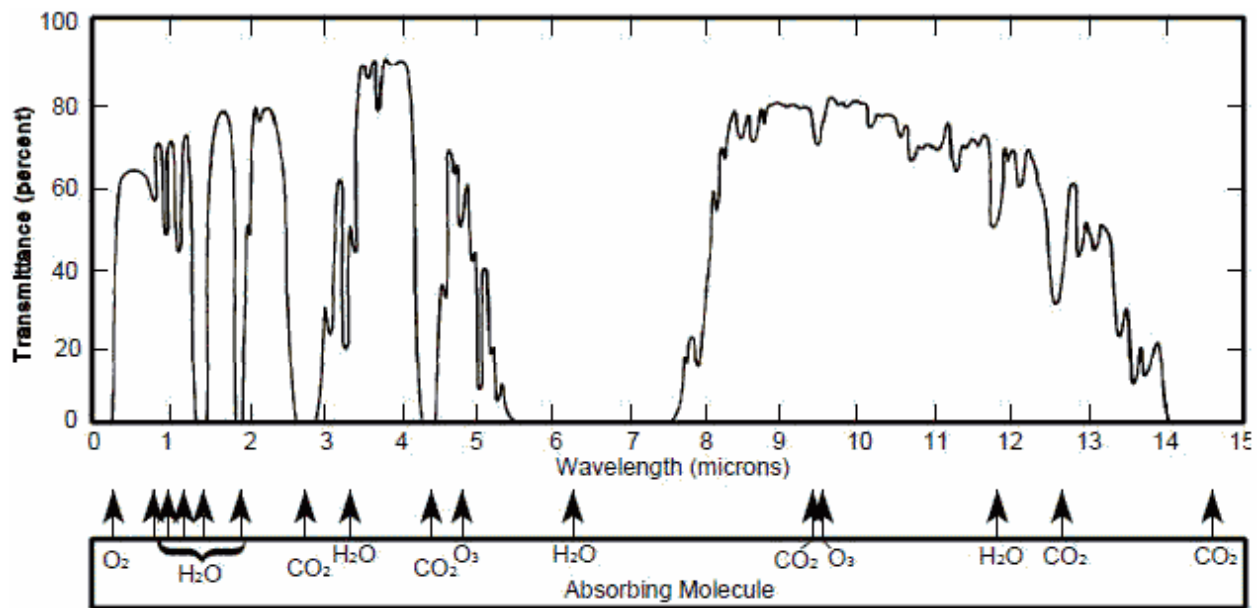


Figure 2.3: Atmospheric transmission spectrum [1]. Public Domain.

The bands can be further categorized into reflective and emissive bands. The wavelengths emitted by the sun define which bands are reflective, as they reflect off terrestrial objects and can be detected by EO/IR sensors. The sun peaks in the visible wavelength band and has detectable signal on earth out to the MWIR.

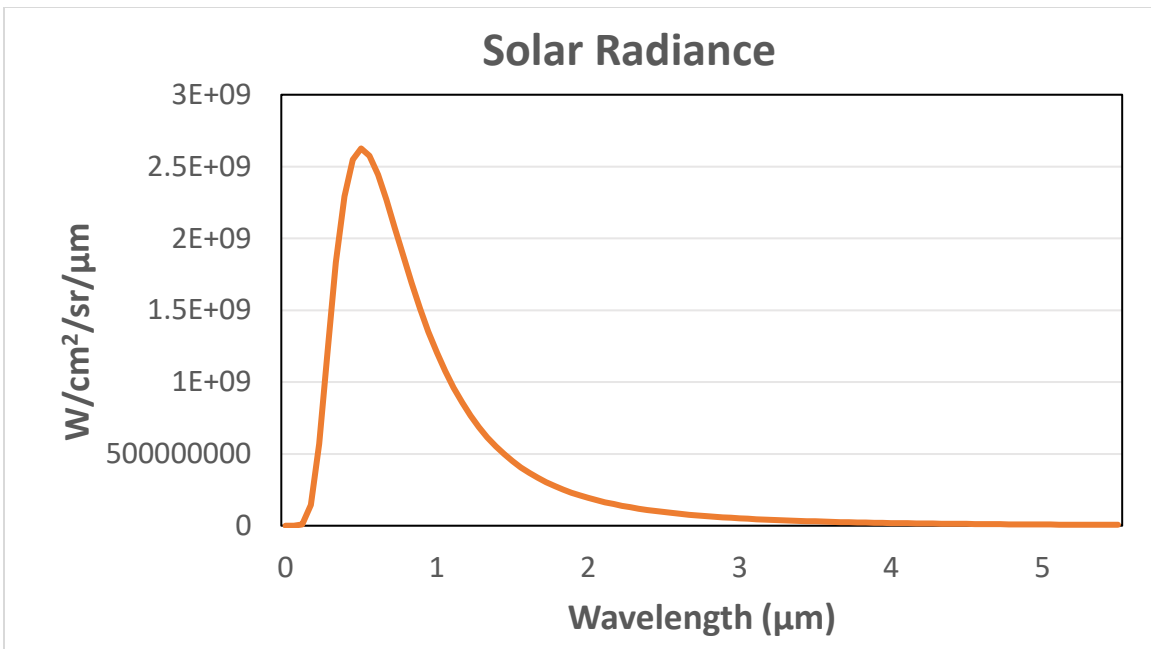


Figure 2.4: Solar Radiance Curve

The wavelengths emitted by the cooler objects on earth define the emissive bands. For a terrestrial object with a temperature around 300K, radiance peaks in the LWIR around 10 microns in accordance with Wien’s law and emits detectable radiation out to the MWIR.

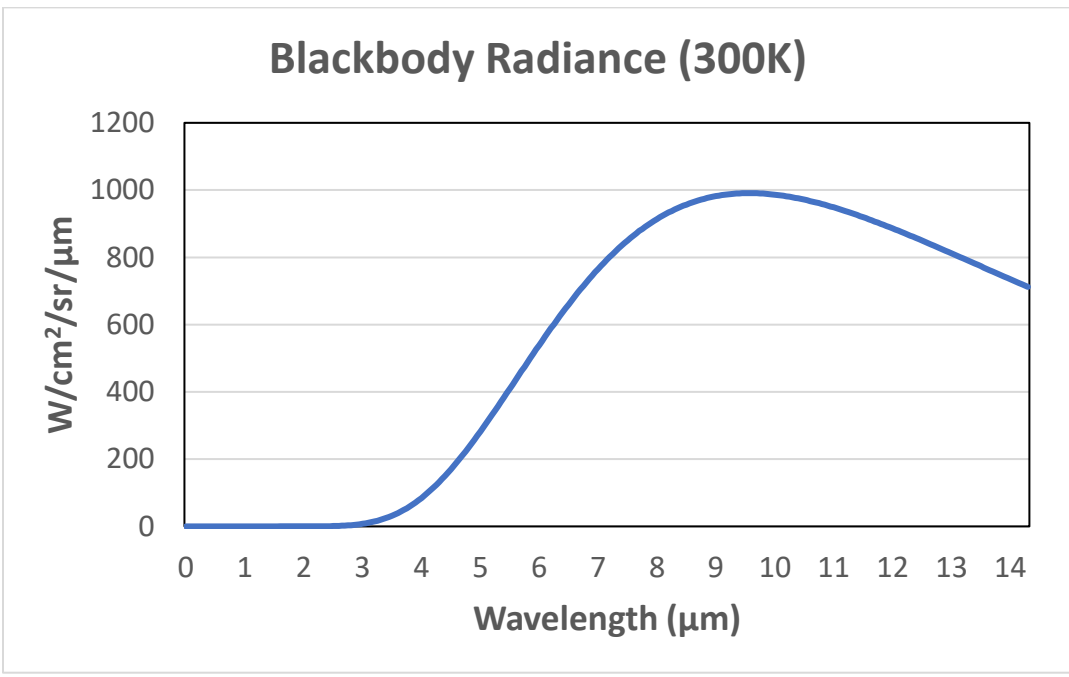


Figure 2.5: 300K Blackbody Radiance Curve

Sensing electromagnetic radiation in different bands provides valuable information about the world around us. The radiation contained within each of these bands has different properties, and imaging different bands yields different information. The band that provides the optimal information is not always the same between different applications, and choosing a band which provides the most information about a given scene is one of the most important decisions when designing an EO/IR sensor.

## **2.2 Infrared Imaging**

EO/IR systems are designed to convey information contained in a scene to a user. This information originates from the scene, where photons are either reflected or emitted by the objects in the scene. Information is not contained in the photons themselves, but in the spatial variations in radiance caused by variations in depth, temperature, irradiance, and material. The progression of information through a system is shown in Figure 2.6. Photons must first pass through the atmosphere to the optics, where they are imaged to a detector. When photons strike a detector, electrons are sent into the electronics of the system which are processed and displayed as an image. Each of these steps results in both a loss in spatial resolution of the information, and a loss of sensitivity to small variations in radiance.



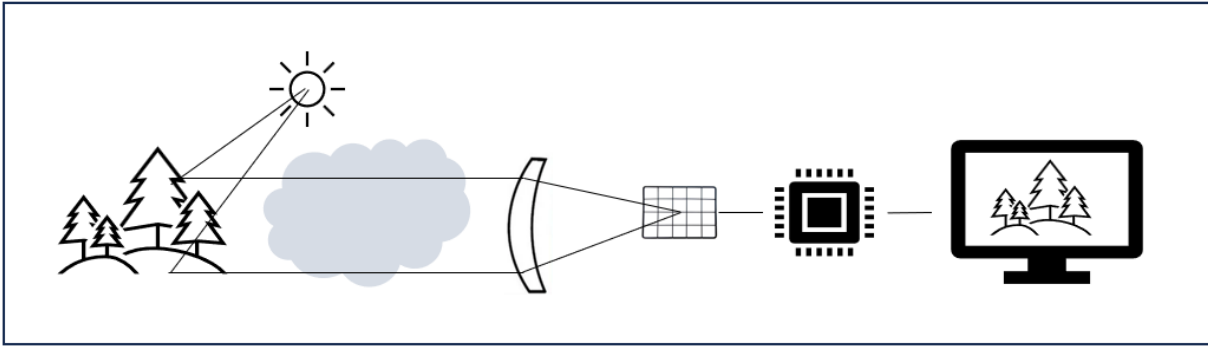


Figure 2.6: Progression of information through an EO/IR system.

The resolution of a system is defined by the modulation transfer function (MTF). The MTF of a system describes loss of contrast in the resulting image as a function of spatial frequency of the scene. More contrast is lost at higher spatial frequencies, and less contrast is lost at lower spatial frequencies. There is an MTF associated with each element of the system, and each MTF is multiplied together resulting in a system MTF. Optics create a blur in the system due to diffraction (blur proportional to the ratio of the wavelength and the diameter of the aperture) and aberrations. Detectors create another blur due to spatial quantization of detector elements and sampling frequency limitations due to this quantization. Low resolution is manifested as a blur in the resulting image.

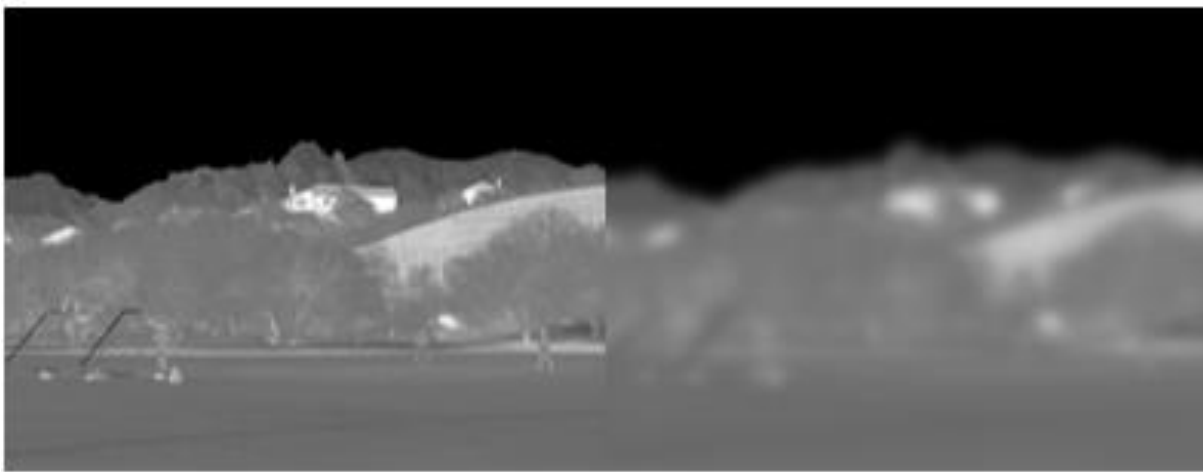


Figure 2.7: Higher-resolution image (left) and lower-resolution image (right)

Figure 2.7 depicts an image of a scene with high resolution, and a corresponding scene with low resolution. The low-resolution image is seen as blurry, as there is no longer contrast in the higher spatial frequency components of the image. The contrast in the low spatial frequency components, such as the contrast between the sky and the ground, stays constant.

Sensitivity describes the smallest change in radiance from a scene that can be detected by the system. Sensitivity is degraded through both loss of signal and generation of noise. As the signal from the scene passes through the atmosphere and the optics, a portion of the photons are scattered, reflected, or absorbed and this signal is lost. Once the transmitted photons strike the detector, a certain percentage (determined by the quantum efficiency (QE) of the detector) of photons generate electrons which subsequently fill up a capacitor “well.” The electronics of the system send a signal to the display to display a gray value corresponding to the number of electrons detected in the well.

There are constant random variations (noise) in the signal detected by the electronics. First, the photons generated by a single element of the scene follows a Poisson distribution; the random variation in photons generated corresponds to the square root of the mean photons generated. The detector generates dark current due to thermal energy contained in the sensor; this also follows a Poisson distribution and has noise corresponding to the square root of the electrons of dark current. Reading the electrons from the detector to the electronics generates a baseline level of noise as well. Total noise is calculated by taking the root sum square of each individual noise source.

Basic gain in an EO/IR system multiplies the number of electrons captured in a well. This is useful when the strongest signal in a scene does not come close to filling the well; multiplying this signal stretches the dynamic range of the imager across the display such that smaller signals result in greater gray levels in the resulting image. It should be noted that the noise electrons are multiplied

as well as the signal; when the small dynamic range is stretched, noise is amplified. Another way to influence the dynamic range of an EO/IR system is the offset level. For scenes with a minimum signal level that is not close to zero, a new “zero” can be set where a certain number of electrons in the well correspond to black on the display.

Signal-to-noise ratio (SNR) is a good measure of whether a feature in a scene can be discerned or not. Low SNR indicates high noise and low signal; it is difficult to distinguish between random variations in detected signal and real variations in signal. High SNR indicates low noise and high signal resulting in a clean image.

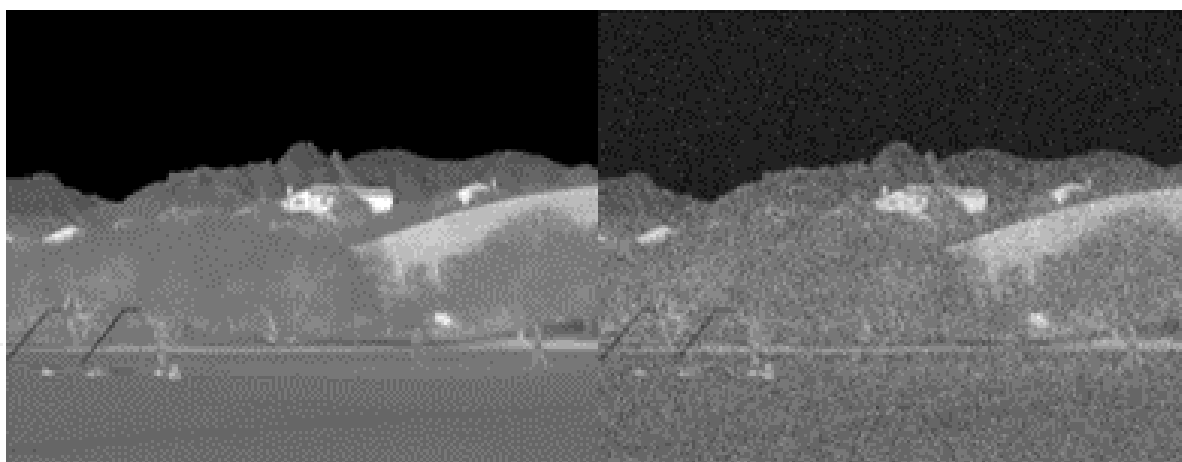


Figure 2.8: Higher SNR image (left), lower SNR image (right)

Figure 2.8 depicts an image of a scene with high SNR, and a corresponding scene with low SNR. In the high SNR image on the left, it is possible to distinguish between small differences in signal (e.g. the trunks of the trees and the background). In the low SNR image on the right, large differences in signal can still be distinguished between (e.g. the sky and the mountains) but smaller differences are drowned out by the noise. The image on the left has higher sensitivity.

One model used to calculate and predict the performance of infrared systems is Night Vision Integrated Performance Model (NVIPM). NVIPM uses the Targeting Task Performance (TTP)

metric to calculate the probability of detection, recognition, and identification of a target at range. TTP takes both the resolution and sensitivity of an imager into account to determine the performance. The equation for TTP is as follows [1]:

$$TTP = \int_{\xi_{low}}^{\xi_{cut}} \left[ \frac{C_{TGT}}{CTF_{sys}(\xi)} \right]^{\frac{1}{2}} [cycles] \quad (4)$$

Where  $\xi_{cut}$  and  $\xi_{low}$  bound the spatial frequencies present in the scene,  $CTF_{sys}(\xi)$  is the system contrast threshold function, and  $C_{TGT}$  is the contrast of the target. The CTF of the system describes which frequencies can make it through the system and be detected by the human eye.  $CTF_{sys}(\xi)$  is as follows:

$$CTF_{sys}(\xi) = \frac{CTF_{eye}(\xi)}{MTF(\xi)} \left( 1 + \frac{\alpha^2 \sigma^2(\xi)}{SCT^2} \right)^{\frac{1}{2}} [unitless] \quad (5)$$

Where  $CTF_{eye}(\xi)$  is the naked eye contrast threshold function (this varies from person to person) and  $MTF(\xi)$  is the modulation transfer function of the system, which describes the spatial frequencies passing through the imager. The second half of equation 2 describes noise relative to dynamic range and is governed by the scene contrast temperature (SCT) of the system.  $\sigma(\xi)$  is the noise filtered by the display in Kelvin-root seconds and  $\alpha$  is a proportionality factor (169.6 root-Hertz). SCT is controlled by the gain and offset level of the imager; lowered SCT generally leads to increased contrast at the expense of partial saturation and an increase in relative noise.

The other important part of the TTP equation,  $C_{TGT}$ , is governed by the following equation:

$$C_{TGT} = \frac{\Delta T_{RSS}}{2SCT} [unitless] \quad (6)$$

For any kind of search/targeting/identification application,  $\Delta T_{RSS}$  is the root sum squared contrast in terms of equivalent blackbody temperature. SCT governs the contrast of the target relative to the entire dynamic range of the display.

TTP also has been shown to correlate with perception of general image quality. For applications such as pilotage, where the quality of the entire image is necessary for navigation, TTP has been shown to function as a figure of merit. For an application without a target such as pilotage,  $C_{TGT}$  is set to 1 [5].

### **2.3 What is Scene Contrast Temperature?**

Scene Contrast Temperature (SCT) describes the global variation of the radiance in a scene (within the field of view (FOV) of a system) in radiometric terms for thermal imagers. Vollmerhausen and Jacobs define SCT as “the delta radiometric temperature in the scene needed to generate the average display luminance when minimum luminance is zero [2]”. This definition is consistent with the fact that the thermal image arises from small variations in temperature and emissivity within the scene that rides on a large background radiance. SCT can usually be estimated as the temperature corresponding to half of the dynamic range of the display, although this is false for scenes with irregular statistical distributions of radiance. In simple terms, SCT varies with the highest and lowest radiometric signature in the scene and rises with a larger range of temperatures within the FOV.

Interestingly, a scene with a large spread of object temperatures does not necessarily have a large SCT. Gain and offset level can be used to set dynamic range independently of the signals in the scene, leading to SCT independent of the scene, but this typically loses information in the process and is not standard practice. Instead, gain and level are set such that the coldest object in the scene is at the bottom of the dynamic range and the warmest object in the scene is at the top of the

dynamic range, leading to SCT reflecting the actual range of temperatures in the scene. It is important to note that for scenes including the sky, dynamic range can be expanded using non-linear techniques and the definitions no longer apply as described.

Temperature difference is not a perfect descriptor of the contrast in the scene as the emitted photons from an object are a function of both the temperature and the emissivity of the object. Blackbody equivalent temperature can be used as a descriptor, as it equates the radiance of each object to that of a blackbody emitter (with emissivity equal to 1); any level of radiance corresponds to a specific blackbody equivalent temperature. The standard deviation of the blackbody equivalent temperatures for each of the elements in a scene,  $\sigma_T$  in units of Kelvin, is an indicator of SCT and can be considered a local descriptor. For an imager viewing objects on the ground, the dynamic range is set according to the range of signals coming from the scene; this range correlates with  $\sigma_T$ . For example, a scene with a normally distributed set of signals has 99.7% of the signal is within  $3\sigma_T$  of the mean; if gain and level are set such that the dynamic range of the display is  $\sim 6\sigma_T$ , 0.3% of the scene is saturated and  $SCT = 3\sigma_T$ . For a display dynamic range set to  $4\sigma_T$ , 5% of the scene is saturated but the overall sensitivity of the system increases. This trade off in display dynamic range (sensitivity vs information loss due to saturation) is generally an issue of personal preference for the user, but SCT increases monotonically with  $\sigma_T$ ; this trend is true regardless of the statistical distribution of signal across the scene.

There is an argument to be made that the range of a set of equivalent blackbody temperatures is a better indicator of intrinsic SCT than the standard deviation of the set of equivalent blackbody temperatures. Range is directly analogous to SCT and represents the true range of radiance from the scene, however it does not account for outliers or trends within the dataset. For scenes with small areas with extremely high or extremely low radiance, the range would be larger than it should

be to realistically represent SCT in a real application, since these small areas would be allowed to be saturated. Additionally, if the dataset has a large range but almost all values are grouped around the mean, SCT would be set such that contrast is maximized for data near the mean. The standard deviation metric accounts for variations like this and is a better representation of SCT.

While there are spatial characteristics of the scene which correspond to high clutter, the SCT describes the amplitude of the scene corresponding to the signals that compete with the target signature [4] when linear contrast stretching is based on global contrast. Some scenes with high SCT and many objects in the scene that are close to the target size would be considered “high clutter” scenes. For these scenes,  $\sigma_T$  can capture the clutter complexity.

Figure 2.9 shows an example of two scenes with high and low  $\sigma_T$ , and the effect of SCT on display sensitivity and saturation. For the scene with low  $\sigma_T$ , a low SCT reveals differences in temperature with much higher contrast than a high SCT. For the scene with high  $\sigma_T$ , a low SCT reveals temperature differences with extremely high contrast but loses information outside of the dynamic range due to saturation.

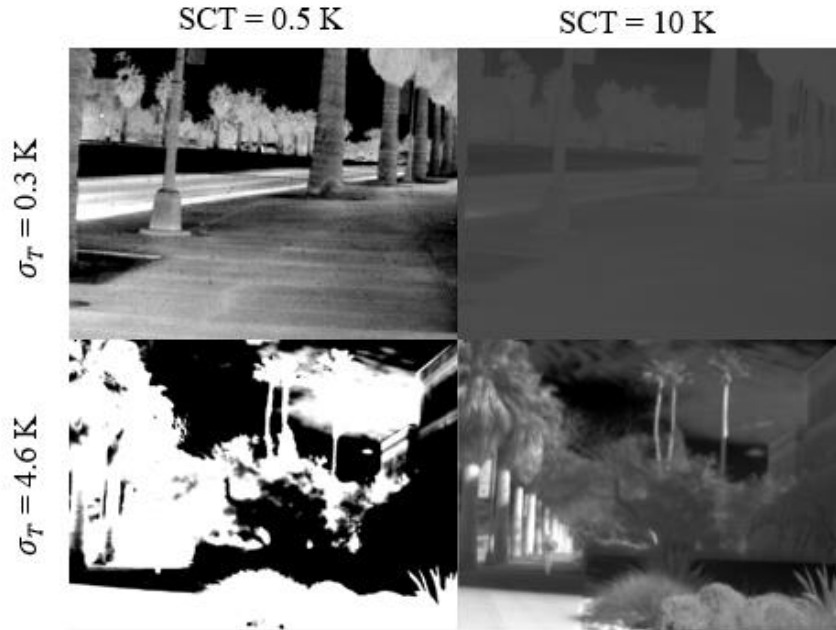


Figure 2.9: Images depicting effects of variation in SCT and  $\sigma_T$  (low SCT right, high SCT left, low  $\sigma_T$  top, high  $\sigma_T$  bottom)

The definition of SCT is based on linear contrast stretching and the assumption of a display dynamic range as perceived by an observer. This definition is a global definition of SCT.  $\sigma_T$  is a local descriptor of scene contrast and depending on the scale, can be used to discuss the effect of clutter in the scene or the effect of the scene contrast in other applications such as pilotage, and GPS-denied image-based navigation. When discussing SCT or  $\sigma_T$  in the context of a scene, we are really discussing the variation in radiance within the scene.

## 2.4 Importance of SCT

Fluctuations in SCT cause variation in the dynamic range of the imager display. The larger the dynamic range is, the less apparent small changes in temperature are and the noise is less significant compared to the signal from the scene.



SCT influences the performance of different applications differently. High SCT and high  $\sigma_T$ , can cause a reduction in performance for some sensor applications such as target detection in the wide field-of-view (WFOV) search task and target identification in the narrow field-of-view (NFOV). Low SCT and  $\sigma_T$  causes a reduction in performance in other sensor applications such as pilotage performance or GPS-denied, image-based navigation.

Pilotage systems are designed to give operators enhanced situational awareness, especially at nighttime and in degraded visual environments. SCT provides a description of the scene contrast in conditions that pilots fly in, and the conditions can vary significantly. The Targeting Task Performance (TTP) metric is designed to quantify the performance of a targeting system but is also used to quantify the performance of a pilotage system as a function of SCT [5]. This equation compares the noise in the system to the SCT. The TTP metric increases logarithmically with SCT at extremely low SCTs.

A pilot can more easily distinguish between objects in the scene with high  $\sigma_T$  and therefore high SCT. Situational awareness is enhanced because when  $\sigma_T$  is much greater than the sensor noise, as this leads to a higher SCT and noise taking a very small part of the dynamic range of the display. This advantage due to increased SCT is “capped” once the noise is negligible compared to the dynamic range. Figure 2.10 shows a typical pilotage performance plot of TTP value as a function of SCT with four examples of possible pilotage images.

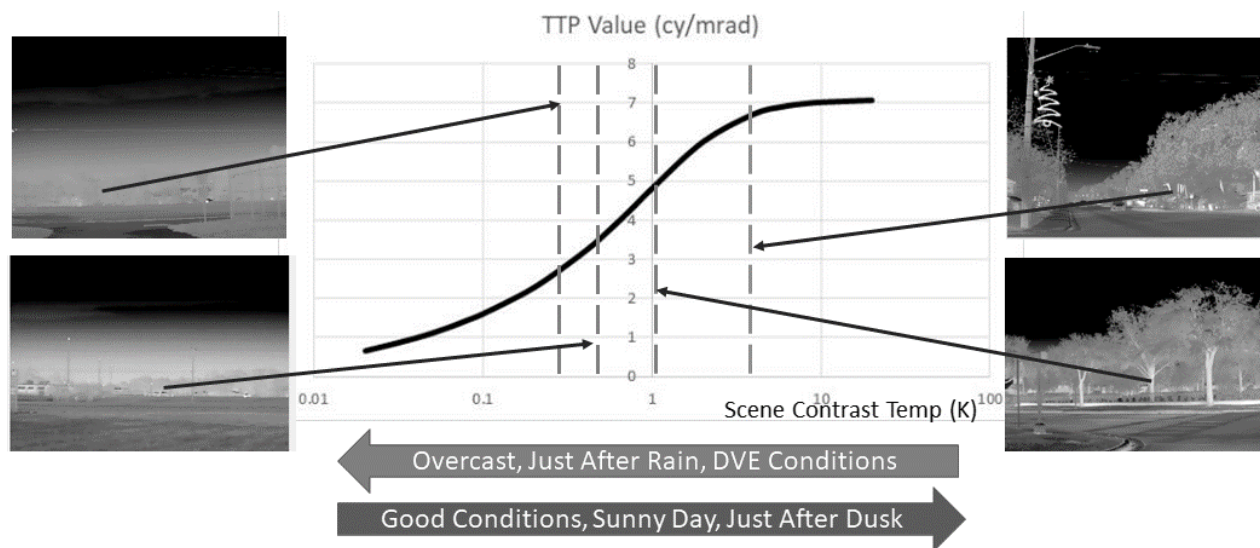


Figure 2.10: Typical Pilotage Sensor Performance Curve as a function of SCT. Example images correspond to dotted lines.

There are four figures near the pilotage TTP plot where the SCT of the terrestrial part of the scene (not including the cold sky), is 0.2K in the upper left, 0.5K in the lower left, 1K in the lower right, and 3K in the upper right. Each example image corresponds to a single SCT and a resulting TTP value as indicated by each dotted line. The pilotage performance curve reduces with a lower SCT and, at some point, the TTP is low enough that it is not safe to fly.

The second case where a high SCT and  $\sigma_T$  are desirable is a recent application when ground vehicles and aircraft are in GPS-denied conditions and images of thermal imagers (e.g., uncooled microbolometers) are compared to a world or regional image database. These comparisons are used to pinpoint the location of the vehicle similarly to GPS. Image correlation and deep learning techniques in autonomous systems are methods used to make these comparisons. In any of these cases, a higher scene contrast provides better signals to be compared to the image databases. Additionally, techniques like Simultaneous Localization and Mapping (SLAM) benefit from higher SCT and  $\sigma_T$  for similar reasons to pilotage and image-based navigation.

Opposite to pilotage and image-based navigation, low SCT in search and targeting is desirable. In search range performance literature [3,4], the target contrast seen by the sensor is:

$$\text{Target Contrast} = \frac{\Delta T_{tgt}}{2SCT} \quad [7]$$

where  $\Delta T_{tgt}$  is the target differential signature in Kelvin. The target contrast equation implies that a larger SCT reduces the target contrast and makes the task of target detection and target identification more difficult when the target  $\Delta T_{tgt}$  remains unchanged. For target identification performance estimates (in a narrow FOV), the apparent SCT is used. The apparent SCT is the SCT propagated through the atmosphere in a manner similar to the apparent target differential signature,  $\Delta T_{tgt}$ . The target and background within the FOV are adjusted to span the display dynamic range. Consider a target with a radiometric temperature difference of 1K, a  $\sigma_T$  of 5K (assuming a user preferring dynamic range of the display to span  $6\sigma_T$ ) leads to a SCT of 15K and a total dynamic range of 30K, with the target spanning 1/30<sup>th</sup> of the dynamic range. For a smaller  $\sigma_T$ , the total dynamic range is smaller, allowing the target to span a larger portion of the total dynamic range.

The two images in Figure 2.11 represent high and low SCT. The image on the left has a low SCT and  $\sigma_T$  (less variation in scene equivalent blackbody temperature) and the image on the right has a high SCT and  $\sigma_T$ .

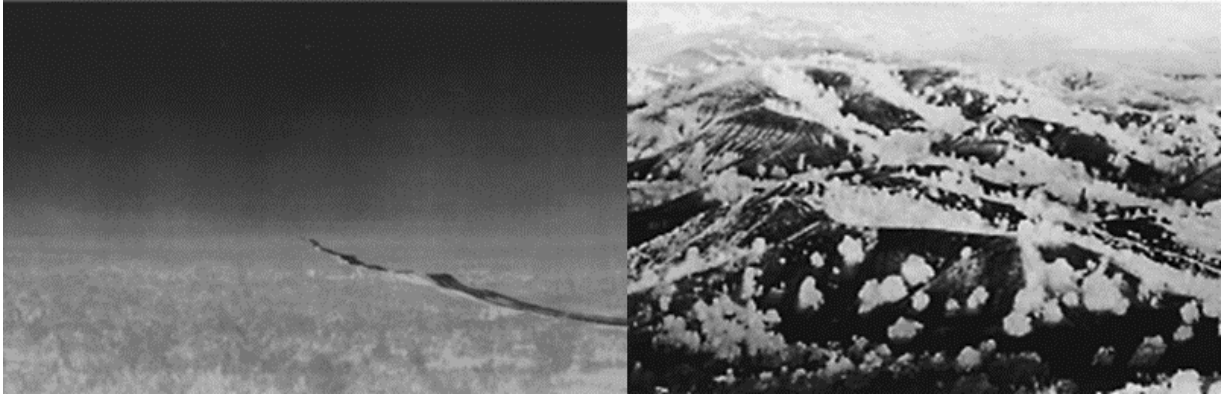


Figure 2.11: Low SCT image (left) and the high SCT image (right)

For a target of low signature, such as a small differential temperature, the target would be easier to find and identify in the left scene as it would span a greater percentage of the dynamic range of the display. SCT has a large influence in many applications and must be considered especially in extreme conditions.

### 2.5 What influences SCT?

The variation in radiance between different objects within a scene is affected by several factors. Variation in emissivity causes variation in emitted photons between objects that are the same temperature in emissive bands. Variation in reflectivity causes variation in reflected photons between objects with the same irradiance in reflective bands. For emissive bands, solar loading increases the variability in temperature between all objects due to differential absorptivity. For reflective bands, differential illumination throughout the scene (shadows) increases the variability in radiance as well.

Low SCT and  $\sigma_T$  correspond to conditions where there is not much thermal variation in the scene, such as after long periods of rainy or overcast weather. High SCT and  $\sigma_T$  are caused by the sun beating the objects in the scene with high thermal capacities for long periods of time. These objects

retain this solar loading over time and re-emit photons as a function of their temperature and emissivity.

This study provides comparisons of mid-wave infrared (MWIR) and long-wave infrared (LWIR)  $\sigma_T$ , and indirectly SCT. The distinction between MWIR and LWIR is very important because this decision is the only method that infrared system designers have to influence SCT.

There are many factors which differentially affect scene contrast in MWIR and LWIR. The sun emits more photons in MWIR and less photons in LWIR. Objects reflect some amount of the MWIR photons from the sun, meaning MWIR has additional scene contrast at daytime due to solar reflections. Objects have wavelength dependent emissivities, and greater variation in object emissivities within a band create higher scene contrast in that band. Additionally, the apparent temperature difference between the sky and terrestrial objects is higher in LWIR than MWIR due to a lower path radiance in the LWIR than the MWIR, meaning that horizon contrast is greater, and reflections of the sky create higher contrast.

This study provides data and analysis comparing SCT in MWIR and LWIR in several different conditions. These comparisons are performed “up close” such that the atmosphere between the sensor and the measured scenes has negligible transmission or path radiance degradation. For longer sensor to scene paths, an “apparent” SCT can be determined, but is beyond the scope of this study.

## **2.6 Previous Research in SCT**

While there is not much work in the literature about quantifying the differences between MWIR and LWIR SCT, there are some small efforts that quantified clutter in the MWIR and LWIR as well as some anecdotal observations about SCT regarding pilotage. In Vollmerhausen’s design

approach to pilotage sensors [7], in one exercise called FROSTY APACHE, the SCT contrast was observed over a period of frequent rain and snow. The SCT was very low, and the background was washed out so that it was difficult to pilot an aircraft. However, a benefit from the low background contrast was that the target acquisition performance of the targeting system was enhanced since warm targets in a washed-out background were easy to find and identify. The targets “popped out” of the background imagery.

At the Kyoto Technical University of Japan [8], researchers measured the SCT of city, forest, mountains, and the sky above the mountains over a period of 10 years. The measurements were taken in all seasons and in various ambient conditions. Their goal was to model infrared clutter, but the bands they selected were 2-3, 3-4, 4-5, and 8-14 micrometers, making it difficult to provide a direct MWIR to LWIR comparison. The measurements showed that the 8-14 micrometers band had more spatial variance than any other band. The 4-5 and 8-14 micrometer bands had consistent spatial variance in the forest regardless of cloud cover or time of day. Also, each spectral band had one or two orders of magnitude difference in variance between daytime and night for most scenes. The purpose of the study was to quantify infrared background clutter. They concluded that the emissive bands provide a Gaussian distribution, and the reflective bands provide a Poisson distribution in radiance.

Georgia Tech Research Institute provided a study [9] that was intended to quantify background clutter [10] in the MWIR and LWIR. They used radiometers on a helicopter looking down on the ground to obtain the data. The spectral bands were 3-5 and 8-12 micrometers. The purpose of the study was to quantify clutter in the two spectral bands and determine how weather, scene type, and measurement conditions changed the clutter. Scenes were classified as open, tree line, or mixed. The classifications were insufficient because important properties of the scene were ignored, and

they used a low pass and high pass filter corresponding to the desired clutter sizes. With these caveats, there were some useful observations from the effort. The MWIR and LWIR data did not show the same behavior regarding spatial variances. The diurnal data showed that both bands peaked in the middle of the day with solar reflections and solar loading. The variations were less at night, but the variations for MWIR were more consistent than LWIR. Overall, the data showed that LWIR variance was higher than MWIR, but that the MWIR was less susceptible to environmental changes. There were no measurements in precipitation related to rain or snow.

Thermal crossover occurs due to the natural diurnal cycle of ambient temperatures. Solar loading causes objects to heat up during the day and objects in the scene retain different amounts of solar radiation. After sunset, the air temperature drops, and the objects cool off while emitting their solar loaded energy. Eventually, all objects are at similar temperatures and the scene has low contrast. Thermal crossover is considered a “worst case” for pilotage systems that must use this contrast for terrain-following night flights. For Vollmerhausen’s development of the TTP metric for pilotage performance involved a study [6], where backgrounds were segmented for two cases (boxes of interest): the horizon and below the horizon. In the study, the standard deviation of the pixel values in the box were compared for the MWIR and LWIR spectral bands. Thermal crossover was prevalent mainly for scenes that included the horizon. The table below shows the results in terms of the LWIR to MWIR ratio of the standard deviation measurements.

Table 1. Vollmerhausen and Bui Results from [6].

Image at Horizon	1	3	5	7	9	11	13	15	16	18
LWIR/MWIR Ratio	2.5	2.6	3.5	2.4	5.3	2.8	1.8	2.3	2.0	3.5
Image Below Horizon	2	4	6	8	10	12	14	17	19	20
LWIR/MWIR Ratio	1.0	0.8	1.1	0.9	1.1	0.9	1.1	1.7	1.1	1.2

Images below the horizon tended to provide nearly equal contrast regardless of where the images were acquired. These results did not agree with the results from [8], but the bands were quite different. A larger factor is that Vollmerhausen and Bui compared the contrasts in equivalent blackbody temperatures and the Kyoto study compared contrast in radiance. A description of the comparison between equivalent blackbody temperature, radiance, and conversion to photons/second is provided later in this section.

While the US Army used tree-to-ground contrast as the metric for providing useful imagery [6], the horizon is also another important aspect of pilotage that is critical to the pilotage functions. Note that the LWIR horizon contrast is typically much higher than in MWIR, but the main contributor to this large contrast is the path radiance of the sky (which is always much higher in equivalent blackbody temperature in the MWIR). In fact, sometimes, the LWIR sky-to-ground contrast is a problem in pilotage in that it used a large portion of the scene dynamic range, making it hard to see the smaller contrast features in a scene. In some pilotage systems, dynamic range compression techniques are used to reduce the sky-to-ground contrast in the presented imagery by stretching out the contrast on the ground and compressing the contrast in the sky.

There is some work verifying the importance of SCT. At RDECOM CERDEC Night Vision and Electronic Sensors Directorate [11], researchers conducted human perception experiments to verify different metrics associated with SCT. The goal of the experiment was to compare images with different SCT and measure the perceived image quality. Experimenters adjusted the gain and offset level of different image sets, and mapped target contrast and TTP, two metrics which are shown to directly correlate with SCT, against perceived image quality. The data show that perceived image quality rises as target contrast and TTP are increased, and quickly falls off as features in the scene begin to saturate. As SCT rises, target contrast falls and TTP rises.



## Chapter 3 Theoretical Calculations

### 3.1 Contrast Calculations

For a single scene containing a variety of features (trees, rocks, buildings, roads, etc.). Each of these objects are constantly emitting radiation in the infrared and absorbing sunlight during the daytime. These factors cause the temperature and therefore the radiometric output of each of these objects to vary throughout the day with sunlight and lack thereof. The temperature/emission of an object peaks in the middle of the day after an extended period of solar loading and is at its lowest at dawn. This varies from object to object and scene to scene due to differential absorptivities, emissivities, and solar irradiances.

The actual emitted signal is due to a combination of actual temperature of the objects in the scene as described by Planck's law, as well as the object emissivities. Higher temperature objects emit more photons, and higher emissivity objects emit more photons. Equivalent blackbody temperature describes the radiance coming from an object as equated to the radiance provided by a blackbody (with emissivity of 1) at an equivalent blackbody temperature. The equivalent blackbody temperature accounts for both the actual temperature and the emissivity of the object. Note that emissivity has a spectral component and can change between MWIR and LWIR.

The three ways SCT can be described are equivalent blackbody temperature (as it is reported in this study), watts (W), and photons per second (p/s). Typical equivalent blackbody temperatures for the average background and a typical differential temperature of 1K is given in table 3.1. This differential temperature is converted into differential watts as well as differential photons per second. While this differential temperature could be referring to the target contrast or the scene contrast, the calculated radiometric differences are consistent.

Table 3.1: Comparison of radiometric units and contrast calculations

<b>Parameter</b>	<b>LWIR</b>	<b>MWIR</b>
Spectral Band	8 – 12 $\mu\text{m}$	3 - 5 $\mu\text{m}$
Typical Background Temperature	300K	300K
Typical Differential Temperature	1K (300-301K)	1K (300-301K)
Typical Sensor NETD	40mK	40mK
Background Emittance $\text{W}/\text{cm}^2$	1.202E-2 $\text{W}/\text{cm}^2$	6.21E-4 $\text{W}/\text{cm}^2$
Differential $\text{W}/\text{cm}^2$	1.96E-4 $\text{W}/\text{cm}^2$	2.67E-5 $\text{W}/\text{cm}^2$
Background Emittance $\text{p}/\text{s}\text{-cm}^2$	4.90E17 $\text{p}/\text{s}\text{-cm}^2$	1.13E16 $\text{p}/\text{s}\text{-cm}^2$
Differential $\text{p}/\text{s}\text{-cm}^2$	9.85E15 $\text{p}/\text{s}\text{-cm}^2$	5.11E14 $\text{p}/\text{s}\text{-cm}^2$

For terrestrial scenes, the typical background in equivalent blackbody temperature is 300K for both MWIR and LWIR. A typical contrast temperature is 1K in both MWIR and LWIR. These quantities are useful when using a camera with a noise equivalent temperature difference (NETD) as given in the table (e.g., 40mK), so that a quick signal-to-noise (SNR) ratio is just the target contrast divided by the NETD, which for table 2 is  $\text{SNR}=25$ .

The equivalent blackbody temperatures are converted to a “watt” based radiometry using Planck’s law. These quantities are useful when working with power detectors or detectors that are specified with detectivity. The typical contrast values in table 2 are converted to source emittance given in  $\text{W}/\text{cm}^2$ . The LWIR target contrast rides on a large background temperature power pedestal where contrast between objects is only a few percent of the overall power received from the average background signal. This means that the sensor must have deep wells and detect temperature differences based on small relative differences. LWIR has 8.6 times the target contrast in radiometric power than the MWIR for the same SCT.

For those working with photon counting detectors and cameras, the equivalent blackbody temperatures for the backgrounds and targets/objects can be converted to photon radiometry in emittance. Table 3.1 notes the pedestal of the background as well as the target contrasts in the MWIR versus LWIR in  $\text{p/s}\cdot\text{cm}^2$ . MWIR detectors usually have a smaller capacitor well for collection photo electrons due to the smaller background and contrast. In this case, the number of photons collected in the LWIR is 19.3 times the photons collected in the MWIR. The reason for the larger ratio is that photons in MWIR have more energy than photons in LWIR.

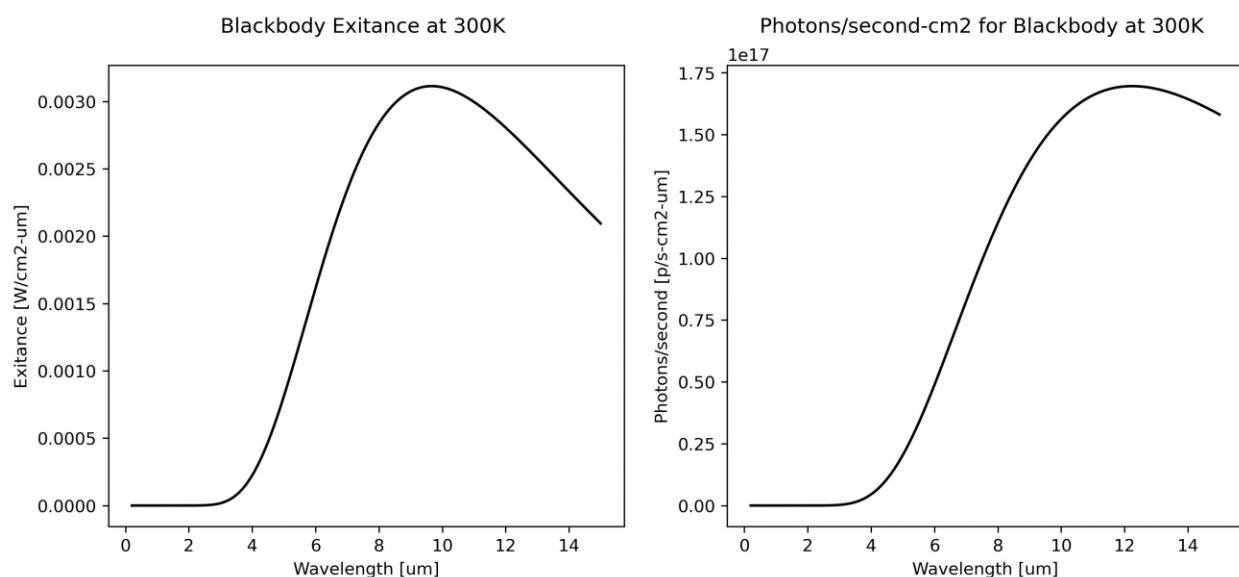


Figure 3.1: Planck's curve for emittance from a 300K equivalent blackbody in  $\text{W}/\text{cm}^2$  and  $\text{p}/\text{s}\cdot\text{cm}^2$ .

Planck's curve for a 300K equivalent blackbody background is shown in Figure 3.1. For a given constant SCT near terrestrial temperatures, the contrast power in watts is just under 10X MWIR versus LWIR. And, in photons per second, the ratio is just under 20X MWIR versus LWIR. This is the reason that MWIR sensors for the same camera design (FOV, detector size, optics, etc.) require a detector integration time of between 10X and 20X longer than LWIR to achieve the same SNR. This limits MWIR in applications that need short integration times in low light scenarios.

### 3.2 Pilotage Performance

This section shows the calculation of the performance of two sample staring array pilotage systems: a LWIR system and a MWIR system. The performance of these systems is calculated as a function of SCT. The specifications of these systems would be optimized for its particular application in practice, but this study does not discuss such optimizations. The imagers are set to be at a 40-degree FOV for a typical focal plane and have low noise. Table 3.2 outlines these specifications.

Table 3.2: Sample pilotage system specifications

<b>Parameter</b>	<b>LWIR System</b>	<b>MWIR System</b>
Spectral Band	8 – 12 $\mu\text{m}$	3 – 5 $\mu\text{m}$
F/#	Varied	Varied
Focal Length	2.11 cm	2.11 cm
Pixel Pitch	12 $\mu\text{m}$	12 $\mu\text{m}$
Frame rate	60 Hz	60 Hz
NETD	20 mK	20 mK

SCT affects the noise parameters of the image as shown in Eq. 5. As scene contrast becomes closer to zero, noise in the sensor becomes more visible in the image and TTP drops. TTP is calculated in a pilotage context (target contrast = 1), using NVIPM for the MWIR and LWIR sensor at F/1 and F/2.

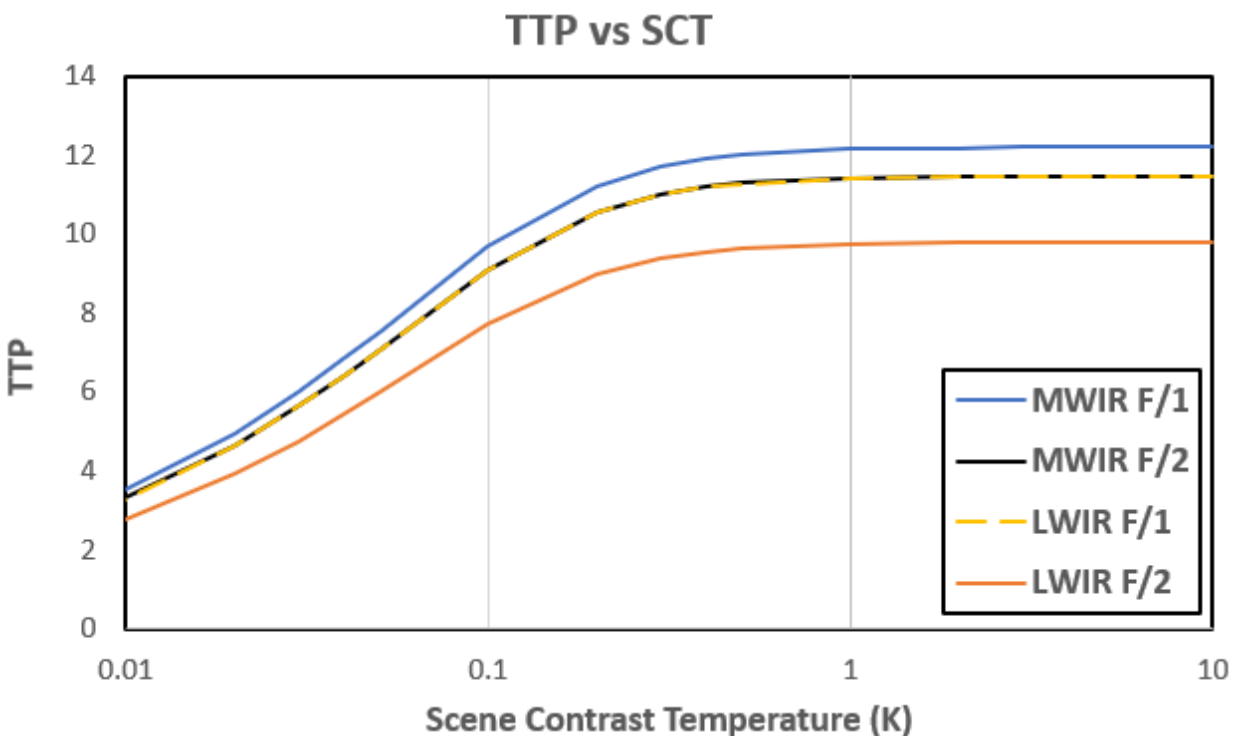


Figure 3.2: LWIR/MWIR TTP vs SCT in a pilotage context ( $C_{tgt}=1$ ) for different F-numbers.

Note the logarithmic scale on the x-axis of Figure 3.2. Above a threshold temperature, TTP does not increase with SCT. Below the threshold temperature, image quality suffers due to noise and TTP drops drastically. SCT is most important in this context when it is very low. A half-degree change in SCT when SCT is near zero can be the difference between good and bad pilotage.

The diffraction blur for a F/2 MWIR system and a F/1 LWIR system is the same, resulting in the same TTP curve for these two systems. If system designers could design faster optics for a MWIR staring array, MWIR would perform better due to decreased diffraction blur as compared to LWIR. It should also be noted that a MWIR system would be required to integrate for much longer than a LWIR system to have a usable signal. There are various other practical limitations

to different system specs that are unique to either band, but this study does not discuss these limitations.

MWIR and LWIR performance are very similar in this calculation; when NETD and blur are equalized, both bands perform similarly. Figure 3.3 shows the performance of the given (F/1) LWIR pilotage sensor as a function of SCT for different NETD values.

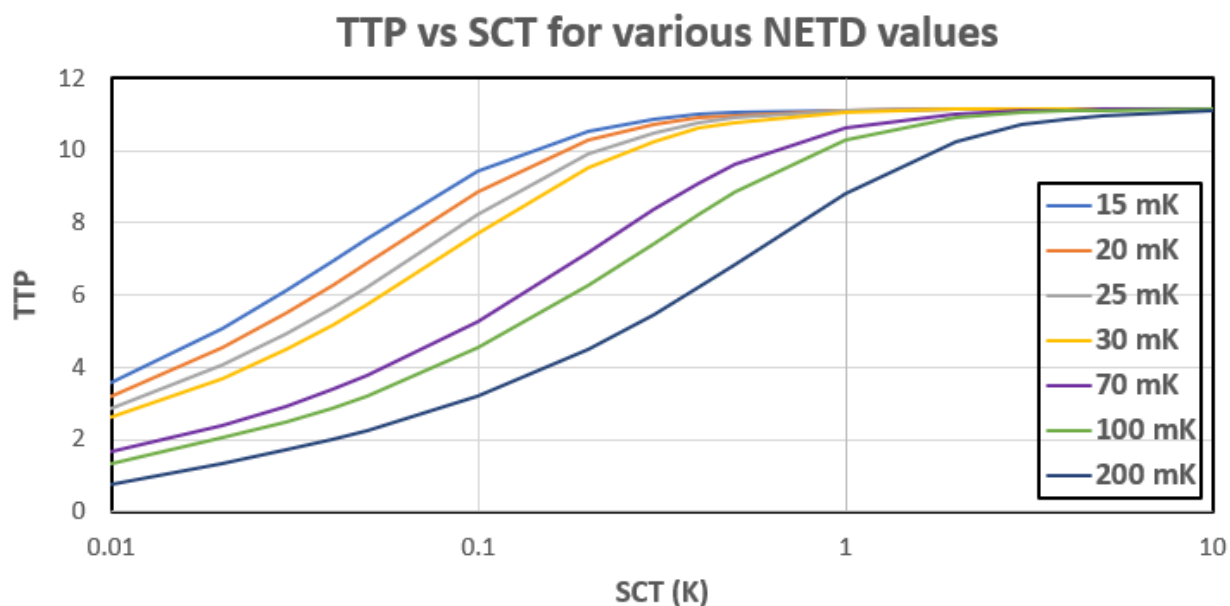


Figure 3.3: LWIR pilotage sensor TTP vs SCT for various NETD values.

In noisier (higher NETD) sensors, the point at which the TTP curve asymptotes is at higher SCT values. This is because the increased noise is large enough compared to the dynamic range at these SCT values to be visible. The noise of less noisy sensors remains small enough compared to lower SCT values to be invisible. At a high enough SCT, neither increased SCT nor decreased NETD increase the final TTP value. This stresses the importance of SCT and NETD in low SCT scenarios, but these factors do not matter to TTP past a certain threshold of SCT.

## Chapter 4 Experimental Description

### 4.1 Goal

The goal of this experiment is to measure the intrinsic scene contrast of scenes in both MWIR and LWIR. These scenes are limited to the ground and do not include the sky. Scenes are varied in time (daytime vs nighttime), contents (urban vs rural), and weather (dry vs humid vs rainy). The dynamic range of our imagers is set to capture all levels of radiance coming from a scene, and this information can be used to calculate  $\sigma_T$ .  $\sigma_T$  accurately reflects intrinsic scene contrast and indicates SCT in both bands for each of the measured scenarios. For each scenario, the ratio of MWIR  $\sigma_T$  to LWIR  $\sigma_T$  is calculated either as a function of time or as an average of all scenes. Equation 8 describes the calculation of this figure of merit (FOM).

$$FOM = \frac{MWIR \ \sigma_T}{LWIR \ \sigma_T} \quad [8]$$

When this figure of merit is above 1,  $\sigma_T$  is greater in MWIR, and when it is below 1,  $\sigma_T$  is greater in LWIR.

### 4.2 Sensors

Two cameras were used to obtain MWIR and LWIR data: a Telops SPARK M150 MWIR camera and a FLIR T1020 LWIR camera. The camera specifications are provided in Table 3. The cameras were converted to radiometers by using a large area blackbody calibration source. To compare scene contrast between MWIR and LWIR, imagery was gathered in multiple scenes from the same perspective in both bands. The output of both cameras was set to be linear with temperature.

Table 4.1: System Information

	<b>FLIR T1020</b>	<b>Telops SPARK M150</b>
Band	8-12 $\mu\text{m}$ (LWIR)	3-5 $\mu\text{m}$ (MWIR)
Format	1024x768	640x512
Pitch	17 $\mu\text{m}$	15 $\mu\text{m}$
FOV	34° x 24°	26° x 21°
IFOV	0.58 mrad	0.71 mrad
NETD	<20 mK @ 30°C	<20 mK @ 25°C
F/#	f/1.2	f/2.3

### 4.3 Calibration

Images were taken by the FLIR T1020 and Telops SPARK M150 mounted adjacently on the same tripod to minimize parallax. The FOVs were aligned such that both imagers were centered on the same scene. Auto-exposure and auto gain were disabled, and the dynamic range was set between the absolute maximum and minimum equivalent blackbody temperatures contained in the scene.

Before taking scene imagery, the two sensors were calibrated such that they both had the same baseline for equivalent blackbody temperature. Two programmable blackbodies (model BB6 from True Colors Infrared Imaging) were positioned such that they were both in the FOV of the MWIR and LWIR cameras and were set to temperatures near the highest and lowest equivalent blackbody temperatures contained in the scene.



Each possible gray level in both LWIR and MWIR images were plotted along their respective equivalent blackbody temperatures. The relationship provided in Figure 4.1 was considered the System Intensity Transfer Function (SITF).

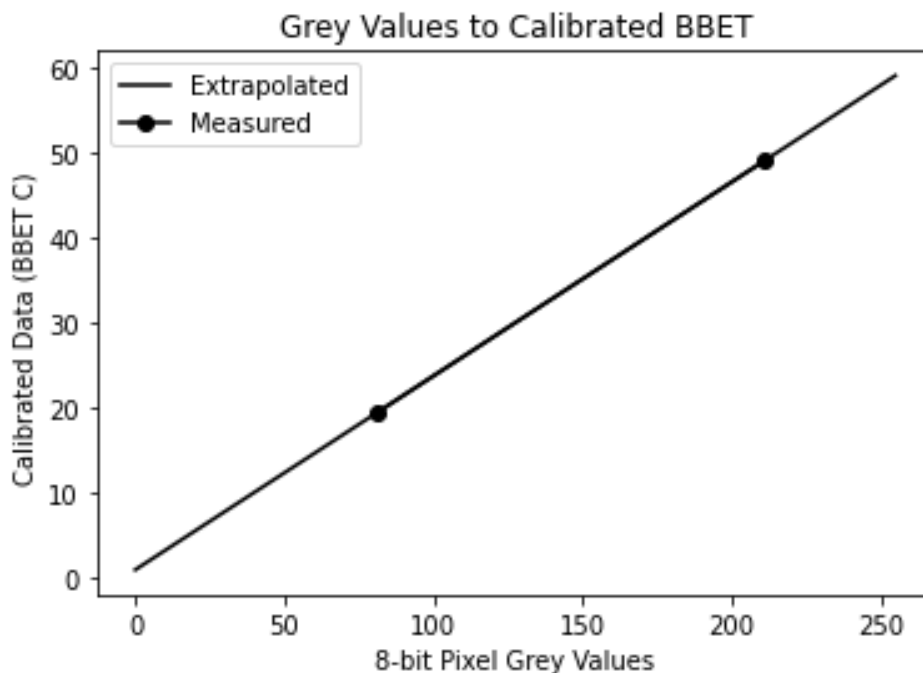


Figure 4.1: Linear relationship of equivalent blackbody temperature to gray level.

Data from the measured scenes were exported into python in .jpeg (8-bit) format, and areas-of-interest were chosen such that the content of the LWIR scenes match the content of the MWIR scenes.

Each area-of-interest is converted into a list of pixel values, and the SITF is applied to the pixel values such that they are converted into equivalent blackbody temperatures, resulting in a list of equivalent blackbody temperatures. These lists are used to calculate the  $\sigma_T$  of each scene. Figure 4.2 shows the two resulting histograms of the conversion of a scene into a list of equivalent blackbody temperatures. These histograms illustrate that there are slight differences between the

different bands in each scene statistically, and these slight differences are what drive the difference in  $\sigma_T$  and ultimately SCT.

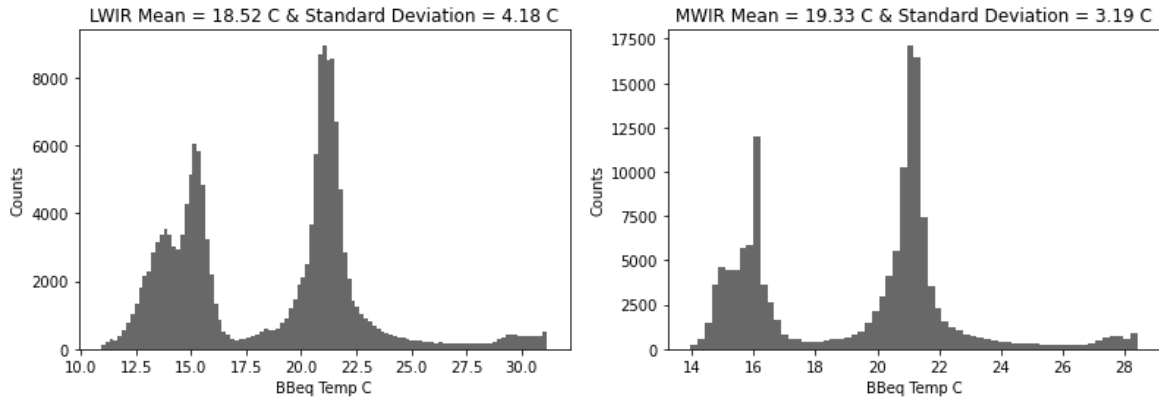


Figure 4.2: Resulting histograms from analysis of a single scene comparison between LWIR (left) and MWIR (right)

#### 4.4 Conditions

To investigate the effects of daytime, a diurnal experiment was conducted where the FLIR T1020 and TEL-7958 acquired images every five minutes for 24 hours. This experiment occurred on a clear day, with the blackbodies in the FOV of the imager for each image taken. The data collection took place in Tucson, Arizona where the climate was high desert in the month of May.

Data was collected in both rural and urban scenes to get a wide variety of content. Rural scene included dry vegetation and rock formations, while urban data included a wide variety of man-made structures and objects. For each rural and urban scene, nighttime and daytime imagery was collected for both the LWIR and MWIR. Data was also collected on a cloudy day so that it could be compared to data collected on a clear day.

Data was collected in a humid environment in Orlando, Florida in the month of November (~60% humidity). Again, the content of the scenes was separated into urban and rural content. Rural scenes, however, contain more foliage and plant life in a humid swampy environment in Florida.

Lastly, data was collected during and after a long period of rainfall in Tucson, Arizona in December. There are a variety of weather conditions during this period (heavy rain, light rain, cloudy, partly cloudy, sunny).

#### **4.5 Sources of Error**

There are several imperfections in this study which cause error. This section discusses the extent of these errors. Due to the nature of the calculation being done, small errors in the image or in the method of calculation become insignificant after taking the standard deviation of the image, and averaging trends over multiple images.

Matching the content between the LWIR and MWIR scene by choosing a similar areas-of-interest is the largest source of error in this study, as there is parallax between the two images, as well as differences in FOV. For a set of sample images, attempting to choose the same areas-of-interest over multiple trials created an average of a 1% error in  $\sigma_T$ . Great care is taken with each image to minimize this error such that it does not affect the overall trend of the data.

The paint used on the blackbodies used has a typical emissivity of above 0.98, therefore an emissivity of 1 is used and the maximum error associated with this imperfect emissivity is calculated. The error in the equivalent blackbody temperature of the temperature of the blackbody source is at maximum (for an emissivity of 0.98) 0.44% of the absolute temperature in LWIR and 0.185% of the absolute temperature in MWIR. The error in the temperature of the blackbodies

propagates to a  $\sigma_T$  error in each data set. For a scene with  $\sigma_T = 3$ , the maximum error in  $\sigma_T$  is 0.8% in LWIR and 0.34% in MWIR.

Another small source of error is the quantization of radiance levels; radiance is measured by both sensors and converted to gray levels as read by the computer. 8-bit imagery (256 gray levels) provides enough dynamic range such that error is insignificant. The statistical trends are well sampled using this dynamic range.

Fixed pattern noise differences between the two cameras create a small amount of error. Noise in both cameras is captured by imaging a uniform source at a very low SCT.

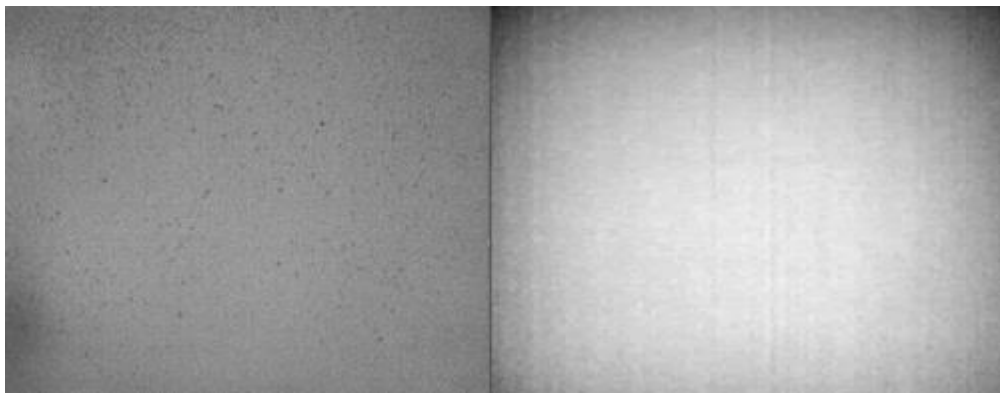


Figure 4.3: Noise depiction (MWIR left, LWIR right)

Fixed pattern noise can be calculated by averaging many frames and taking the standard deviation of the average frame. This fixed pattern noise is 54 mK in the MWIR sensor and 83 mK in the LWIR sensor. The noise is too small to make a significant change in the statistical distribution of measured radiance throughout a scene.

When calculating  $\sigma_T$ , increased magnitude of the variations in radiance within the dynamic range would increase  $\sigma_T$  but would not ultimately affect SCT. It is important to consider this change in radiometric output relative to the total dynamic range in both bands. Since radiometric output is not linear with temperature, the change in signal between two objects in a scene relative to the

whole dynamic range is not linear over all temperatures. Figure 4.4 depicts the relationship between relative contrast within a dynamic range.

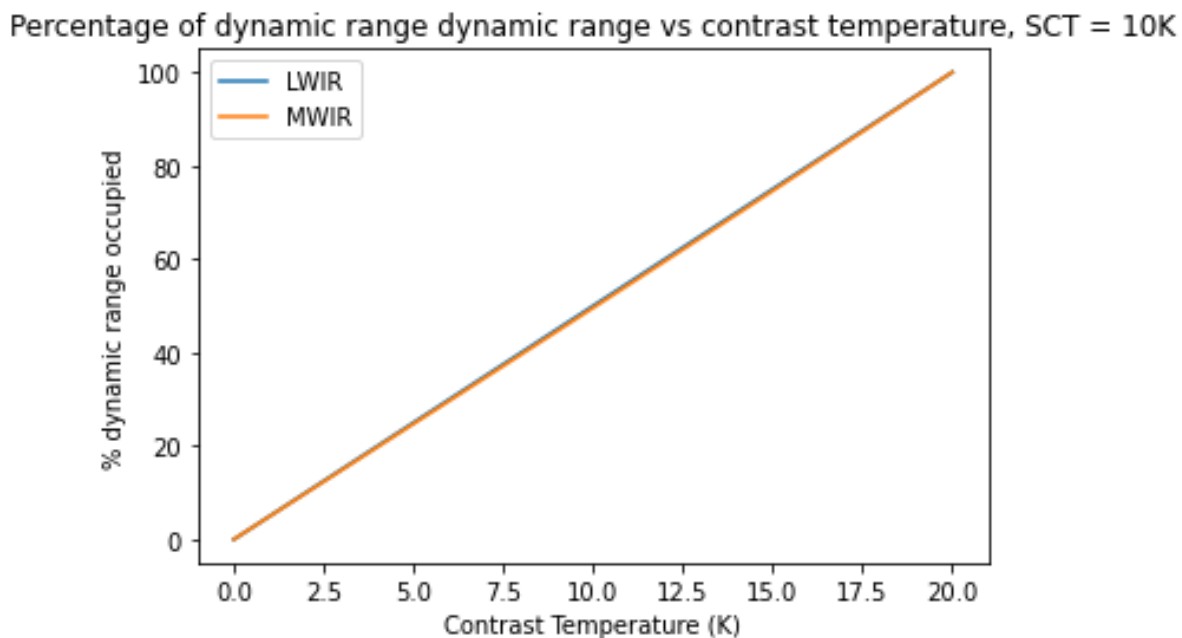


Figure 4.4: Percentage of dynamic range vs contrast temperature, SCT=10K.

For a scene with a normal SCT of 10K, the percentage of dynamic range occupied by a contrast between two objects is linear in both LWIR and MWIR over all contrast temperatures possible in the scene. At much higher temperatures, this linearity does not continue. Figure 4.5 depicts the same relationship at a much higher SCT of 50K.

Percentage of dynamic range vs contrast temperature, SCT = 50K

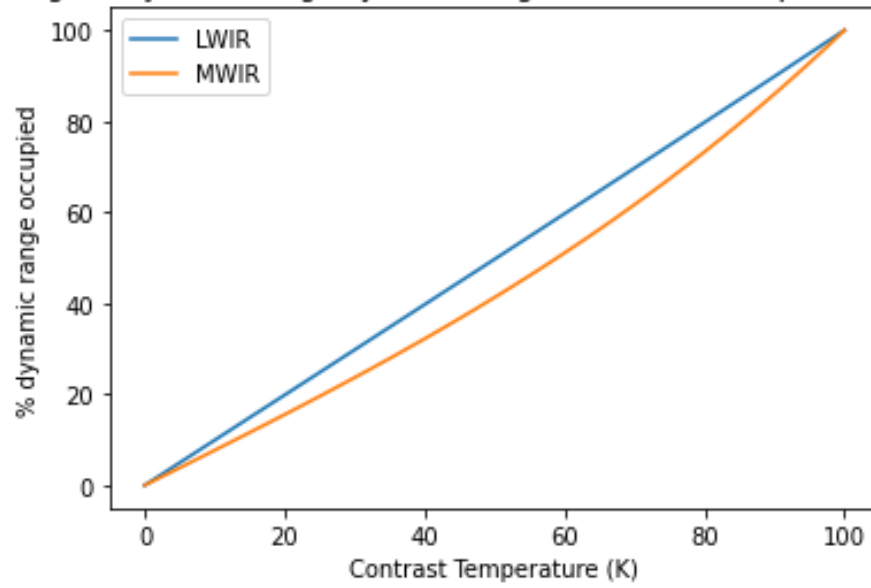


Figure 4.5: Percentage of dynamic range vs contrast temperature, SCT=50K.

When calculating  $\sigma_T$  for typical terrestrial scenes where SCT does not vary this much, this non-linearity may be ignored and  $\sigma_T$  is still a good indicator of SCT.

## Chapter 5 Experimental Results

### 5.1 Diurnal

The SCT and  $\sigma_T$  change with ambient temperature, sun angle, time, and the attempt of all objects in the scene to achieve thermal equilibrium. The sun irradiance and the sun angle have a large effect on both LWIR and MWIR scene contrast due to objects differentially heating up with different amounts of solar illumination and differences in absorptivity. The result of large variations in SCT due to absorbed sunlight is sometimes called solar loading. In addition to solar loading, a significant amount of contrast in the MWIR is due to solar reflections with differential reflectivities and differential amounts of solar illumination reaching different objects. In the LWIR, almost all radiance seen during the day is due to the emitted light. In the MWIR, the radiance seen during the day includes reflected solar illumination which can be a significant contribution to the overall SCT. Reference [12] shows for a sandy surface, the MWIR solar reflections can be 20% to 30% of the SCT signature.

To provide a measure of the diurnal effects, the FLIR T1020 and TEL-7958 were set up to take an image of the same scene every 5 minutes for 24 hours. Samples of the diurnal scenes are shown in Figure 5.1. The top images are in MWIR, and the bottom images are in LWIR. The left side images were taken at daytime, and on the right side were images taken at nighttime. Boxes show the areas that were used in the image analyses. The camera positions were static, and the areas taken in the MWIR and LWIR corresponded to the same scene area.

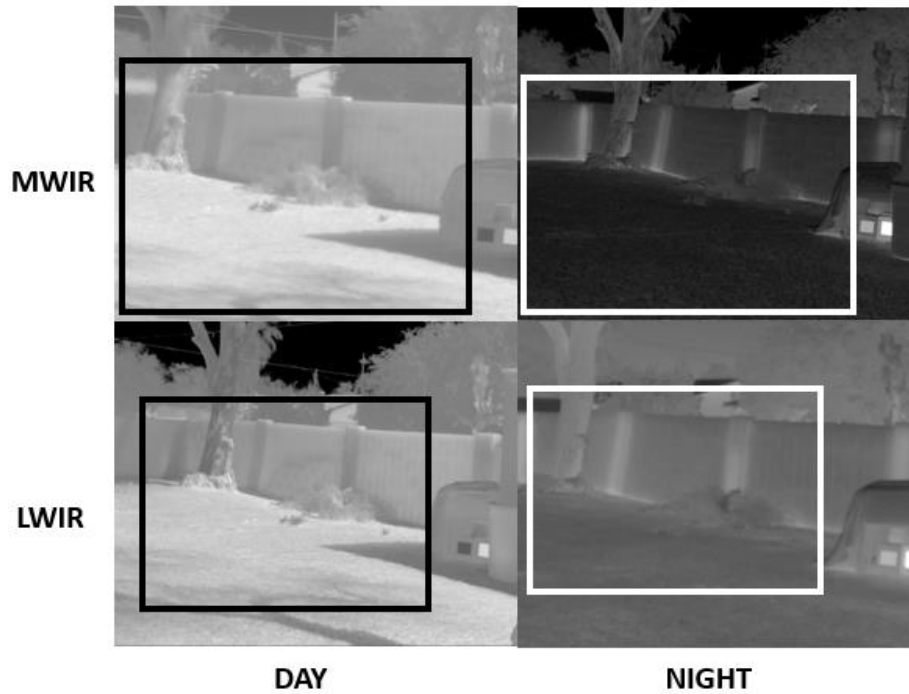


Figure 5.1: Sample diurnal imagery (MWIR top, LWIR bottom; daytime left, nighttime right), boxes show area analyzed.

Figure 11 shows the  $\sigma_T$  for MWIR and LWIR over a period of 24 hours for the scenes shown in Figure 5.1. The diurnal cycle started and ended at 3:20pm. The orange plot corresponds to the MWIR  $\sigma_T$  and the dashed blue dots correspond to the LWIR  $\sigma_T$ . The data was taken from April 8 – April 9 in Tucson, Arizona and the conditions were sunny, clear sky and dry. The maximum temperature on April 8 was 29 C and the maximum temperature on April 9 was 31 C. The humidity ranged between 9% and 32%.



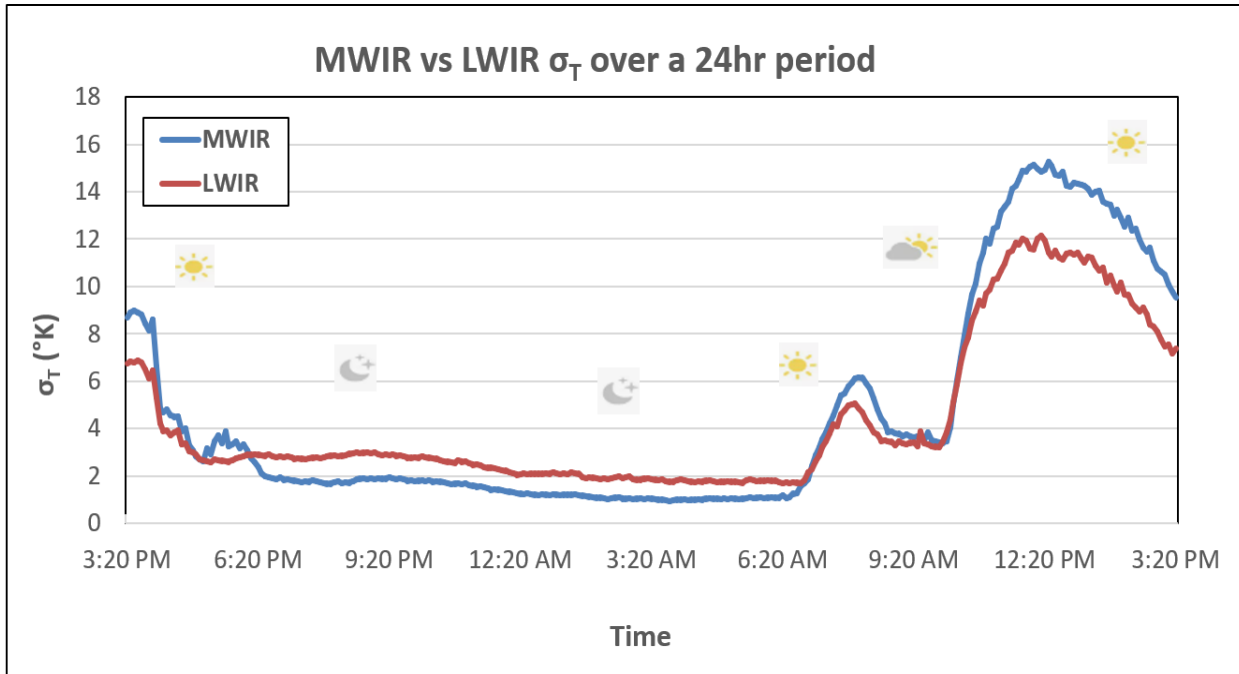


Figure 5.2: MWIR vs LWIR scene contrast over a 24-hour diurnal cycle.

During this nighttime, LWIR  $\sigma_T$  is always higher than MWIR  $\sigma_T$ , where the ratio of MWIR  $\sigma_T$  to LWIR  $\sigma_T$  is roughly 2/3rds through the night. The other aspect of night  $\sigma_T$  is that for both MWIR and LWIR it seems to decrease as the heat of the objects bleeds off towards ambient as the night continues. The lowest  $\sigma_T$  appears just before dawn. During the daytime when the sun is shining, increased radiance variability in the MWIR due to solar reflections increases  $\sigma_T$  in MWIR but not LWIR. During a brief period of clouds,  $\sigma_T$  equalizes for MWIR and LWIR. Figure 5.3 depicts the ratio of MWIR  $\sigma_T$  to LWIR  $\sigma_T$  as a function of time.

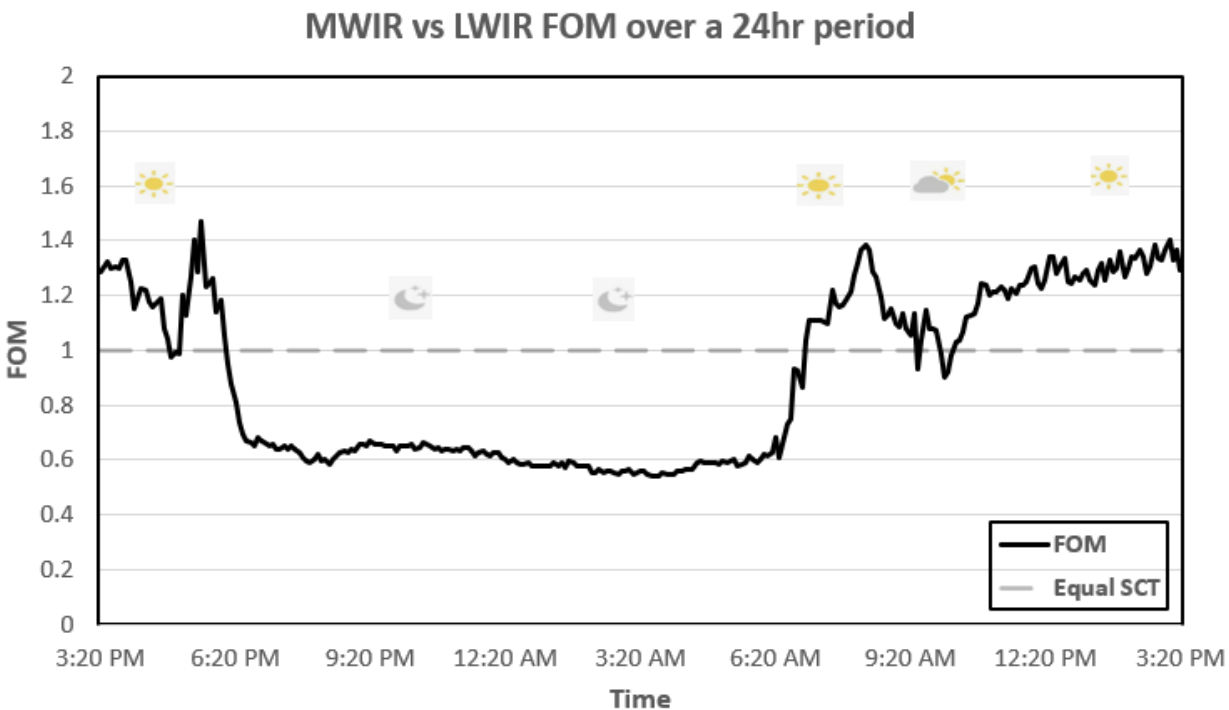


Figure 5.3: Diurnal FOM (Eq. 8) as function of time.

The FOM indicates that there is a consistently large advantage in LWIR  $\sigma_T$  at nighttime, whereas MWIR  $\sigma_T$  has an advantage at daytime only when shadows/clouds aren't present.

## 5.2 Rural

Sample images of scenes from the rural data collection are shown in Figure 5.4. The upper images are MWIR, and the lower images are LWIR. On the left side are images taken at daytime, and on the right side are images taken at nighttime. Boxes are drawn to illustrate the FOV of the LWIR used in analysis to provide the same scene content as the MWIR sensor.

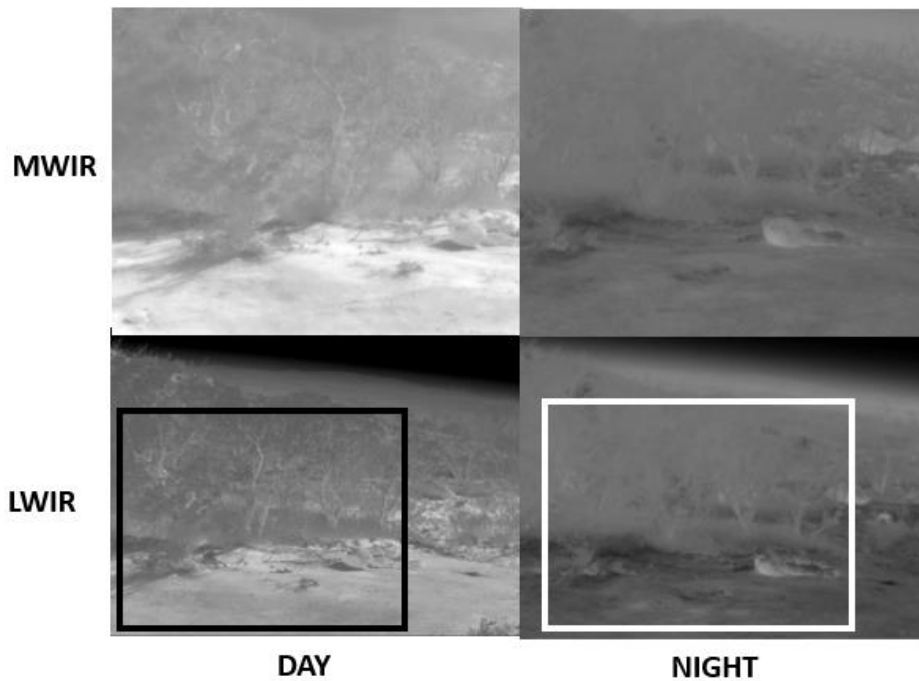


Figure 5.4: Sample rural imagery (MWIR top, LWIR bottom; daytime left, nighttime right), boxes indicate area analyzed.

30 sets of four images are analyzed in rural conditions. The images include both MWIR and LWIR imagery as well as day and night conditions. The  $\sigma_T$  of the scene in the MWIR is plotted against the  $\sigma_T$  in the LWIR for each MWIR/LWIR pair is plotted and shown in Figure 5.5. The diagonal line provides a plot location where the MWIR and LWIR signatures are equivalent. The data points above the line corresponded to greater LWIR contrast and data points below this line corresponded to greater MWIR contrast.

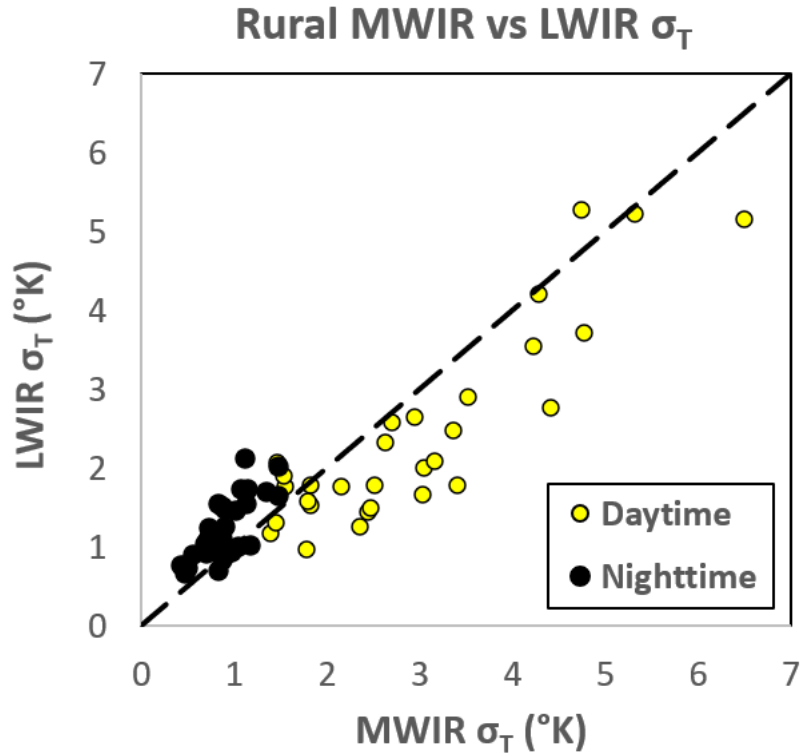


Figure 5.5: Rural scene  $\sigma_T$  distribution for daytime and nighttime

The data show greater  $\sigma_T$  in MWIR at daytime and greater  $\sigma_T$  in LWIR at nighttime. The figure of merit (Eq. 8) is averaged over all nighttime scenes and averaged over all daytime scenes and reported in Table 5.1.

Table 5.1: FOM (Eq. 8) results for rural scenes.

	<b>Daytime</b>	<b>Nighttime</b>
FOM	1.224	0.729

### 5.3 Urban

Sample images of the urban scenes are shown in Figure 5.6. The upper images are MWIR, and the lower images are LWIR. The left side are images taken at daytime and the right side are images taken at nighttime. Boxes are drawn to illustrate the FOV of the images used in analysis and correspond to the same regions of the image in both the MWIR and LWIR. The scenes collected

include manmade park features, buildings, roads, windows, lamp poles, etc. All urban scenes are outside; no inside imagery is used.

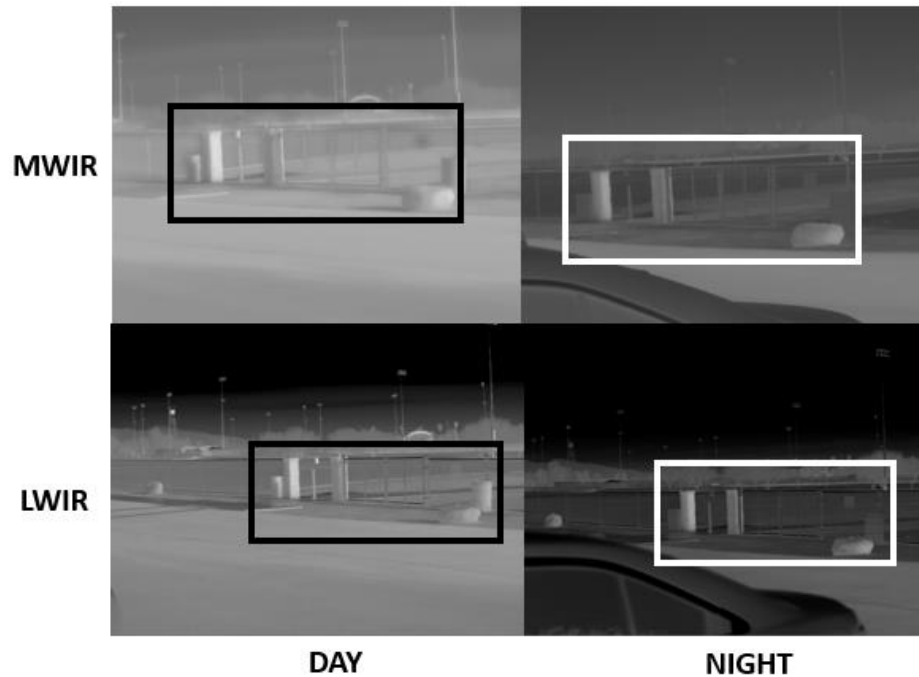


Figure 5.6: Sample urban imagery (MWIR top, LWIR bottom; daytime left, nighttime right), boxes indicate area analyzed.

The day and night results are plotted in Figure 5.7 for both MWIR and LWIR. The diagonal reference is also included in the plot. There was also an opportunity to obtain daytime results with heavy cloud overcast one day and urban data was obtained for overcast cloud conditions.

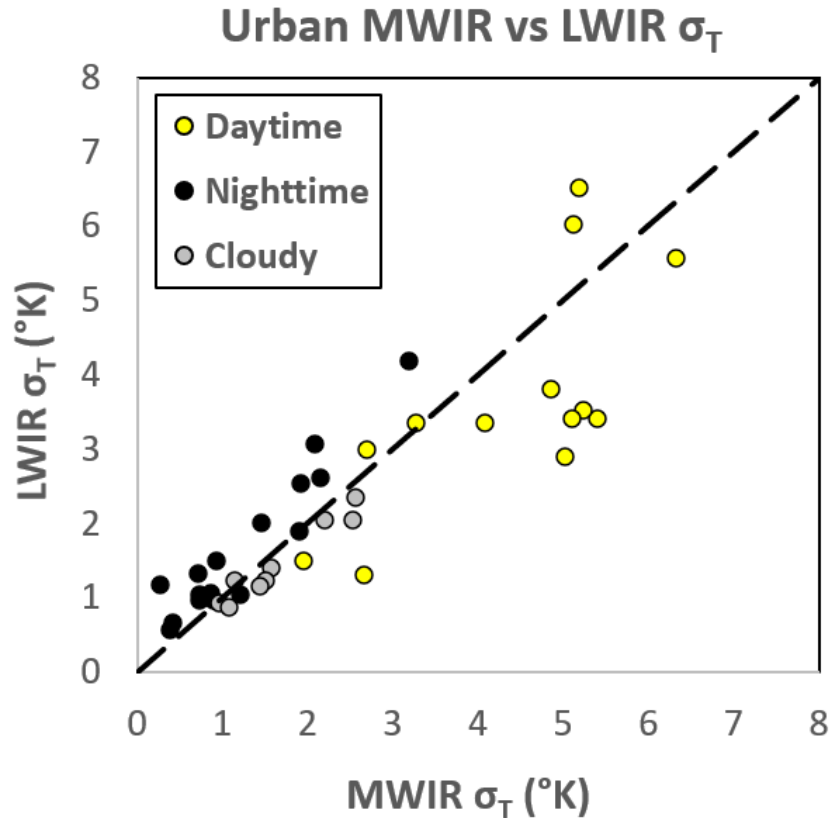


Figure 5.7: Urban scene  $\sigma_T$  distribution for daytime, nighttime, and daytime with clouds

Again, the data show greater  $\sigma_T$  in MWIR at daytime and greater  $\sigma_T$  in LWIR at nighttime.

During a cloudy daytime,  $\sigma_T$  is more equal between the two bands but there is still a slight advantage in MWIR due to sunlight coming through the clouds. The distribution is more irregular than rural scenes because of the variation in content between different urban scenes.

The figure of merit (Eq. 8) is averaged over all nighttime scenes and averaged over all daytime scenes and reported in Table 5.2.

Table 5.2: FOM (Eq. 8) results for urban scenes.

	<b>Daytime</b>	<b>Cloudy Daytime</b>	<b>Nighttime</b>
FOM	1.296	1.138	0.743

### 5.4 Humid Environment

Data is taken in both humid rural scenes and humid urban scenes. To do this, the sensors were taken to Orlando, FL during a sunny, humid week in November. Sample images of the scenes used are shown in Figure 5.8. The upper images are MWIR, and the lower images are LWIR. Urban scenes are shown on the left and rural scenes are shown on the right.

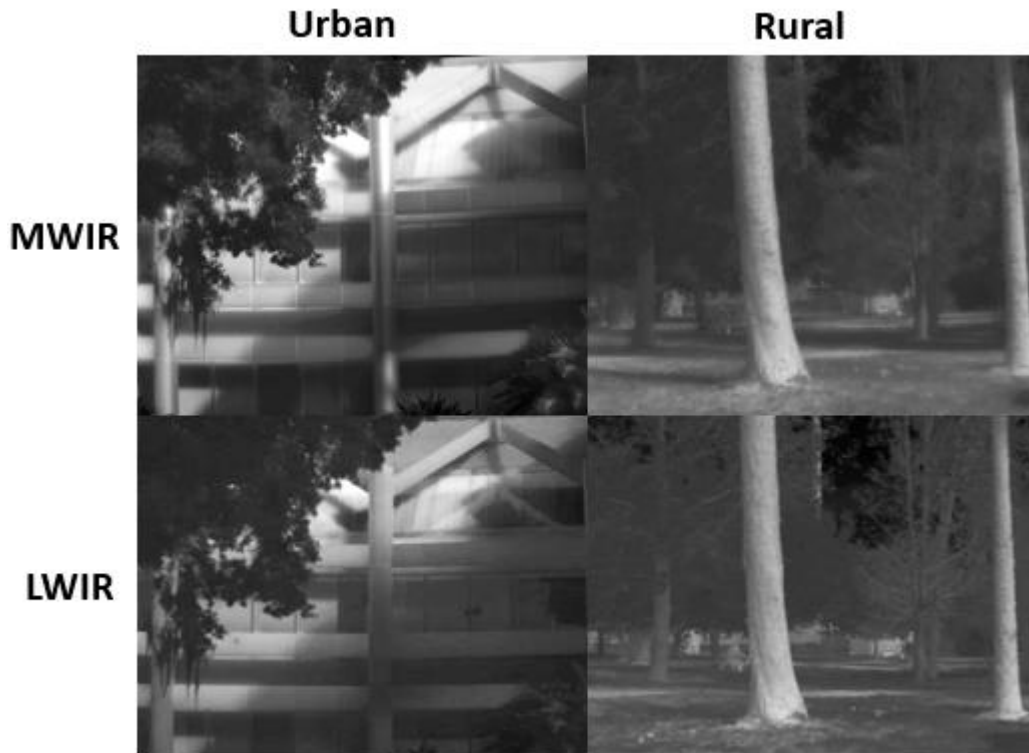


Figure 5.8: Sample humid urban imagery (MWIR left, LWIR right).

The humid MWIR/LWIR results are plotted in Figure 5.9. Rural results are plotted on the left and urban results are plotted on the right. For both plots, the diagonal reference is also included.

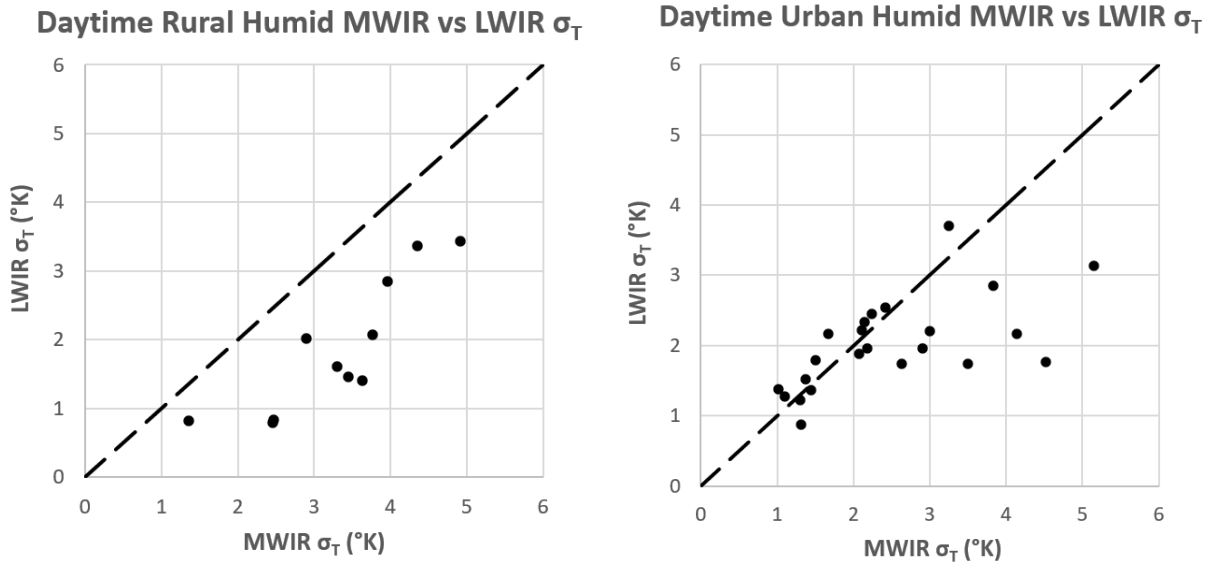


Figure 5.9: Humid rural scene  $\sigma_T$  distribution

The data show greater  $\sigma_T$  in MWIR in rural scenes and slightly greater  $\sigma_T$  in MWIR in urban scenes. The figure of merit (Eq. 8) is averaged over all rural scenes and averaged over all urban scenes and reported in Table 5.3.

Table 5.3: FOM (Eq. 8) results for humid scenes.

	<b>Urban</b>	<b>Rural</b>
FOM	1.235	2.006

## 5.5 Precipitation

Data is taken during a long period of rainfall, and for a long period thereafter in which the conditions return to normal. The scene used is the same one used for the diurnal data. Figure 5.10 shows  $\sigma_T$  as a function of time during a full day of rainfall.



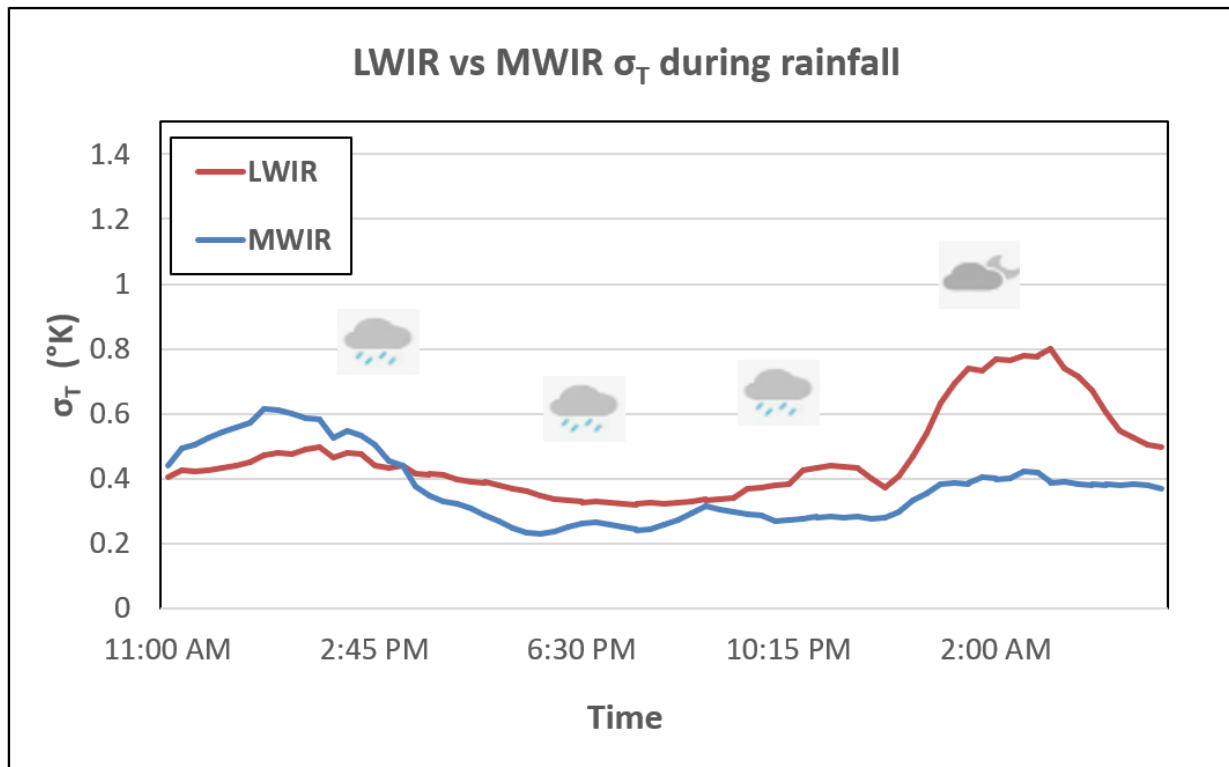


Figure 5.10: LWIR vs MWIR  $\sigma_T$  during rainfall.

Figure 5.10 shows that  $\sigma_T$  is extremely low during rainfall, as rain cools off all objects in the scene to roughly the same temperature, resulting in largely uniform radiance from the scene. Interestingly, at nighttime after the rainfall stops, a spike in LWIR  $\sigma_T$  is seen. This implies that as objects dry off, contrast increases in the LWIR faster than in the MWIR. Figure 5.11 shows  $\sigma_T$  return to normal over a few days after this long period of rain. Figure 5.10 shows a “zoomed-in” view of 22-Dec, the first day shown in Figure 5.11.

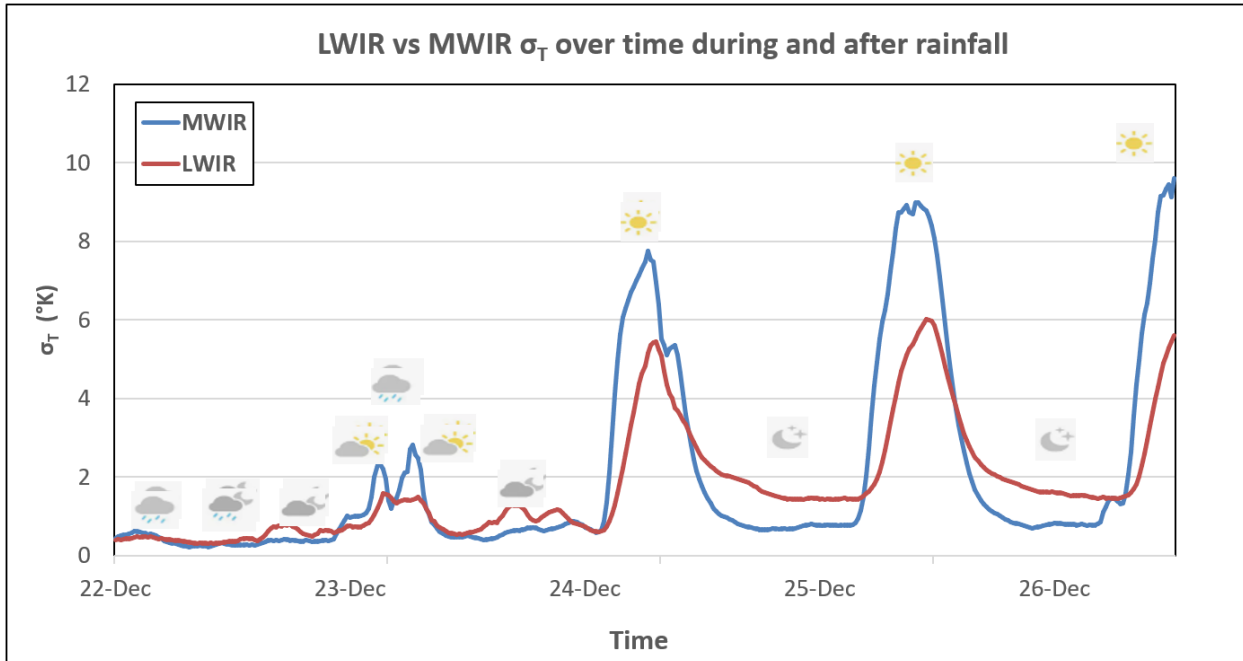


Figure 5.11: LWIR vs MWIR  $\sigma_T$  over time during and after rainfall.

The first day after rainfall shows some slight  $\sigma_T$  recovery, but it remains hampered due to clouds and intermittent showers. During the second and subsequent days after rainfall, solar loading occurs during a large portion of the day and  $\sigma_T$  returns to the normal cycle. The figure of merit (Eq. 8) is calculated as a function of time for the period of 22-Dec to 26-Dec in Figure 5.12.

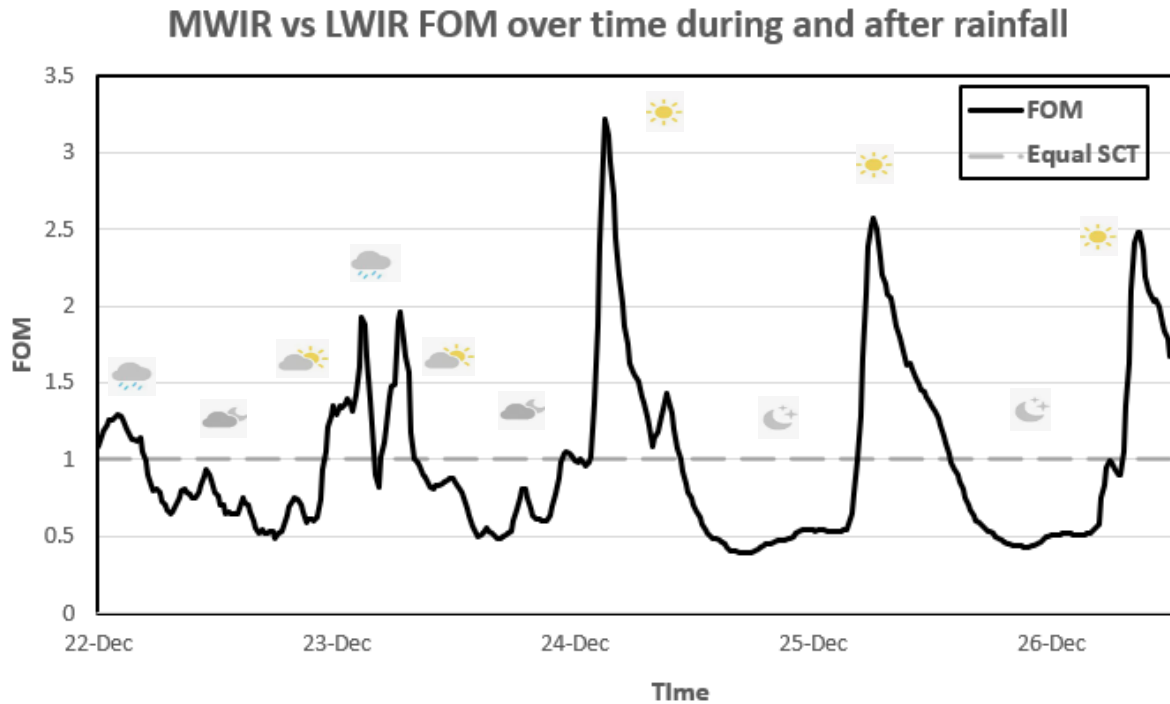


Figure 5.12: FOM (Eq. 8) as function of time during and after rainfall.

The FOM shows much greater peak advantages in MWIR during a sunny day than during the diurnal test, this advantage bleeds off as time moves on. Great spikes in the FOM are seen at the beginning of each daytime, and this is due to a spike in solar reflection which has not heated the objects in the scene sufficiently yet. As solar loading takes place, this spike in MWIR advantage slowly decreases until the following night.

## Chapter 6 Discussion

Time of day, climate, environment, temperature, conditions, and spectral band all play a large role in both MWIR and LWIR  $\sigma_T$  and SCT. Time of day and year influence the amount of solar radiation striking the objects in the scene. This radiation differentially heats up objects with different emissivities, reflectivities, and thermal masses resulting in different  $\sigma_T$  and SCTs. Reflectivity and emissivity are a function of wavelength and therefore also vary between MWIR and LWIR.

The diurnal data showed that the band which has a higher SCT is dependent on daytime. Day  $\sigma_T$  were higher in the MWIR and night  $\sigma_T$  were higher in the LWIR. The ratio of MWIR/LWIR night  $\sigma_T$  was about 0.6 for the entire night. The night  $\sigma_T$  ranged from 1K to 2K in the MWIR and from 1.7K to 3K in the LWIR. In both MWIR and LWIR cases,  $\sigma_T$  reduced as the night progressed and was lowest just before dawn. During the daytime,  $\sigma_T$  became greater in MWIR due to solar reflections increasing the amount of photons coming from the scene. The ratio of MWIR/LWIR day  $\sigma_T$  ranged from 1.2-1.4 for most of the day but dipped down to around equal during periods of clouds or shadows.

For all of the individual scene measurements in different conditions, Table 6.1 provides the ratio of MWIR  $\sigma_T$  to LWIR  $\sigma_T$ . N/A indicates that no data was taken in these conditions, but data taken in other conditions can be used to indicate the trend toward a condition with no data.

Table 6.1: Average FOM (Eq. 8) calculations for each set of individual scene data

	<b>Daytime</b>	<b>Nighttime</b>	<b>Cloudy Daytime</b>
Rural	1.224	0.729	N/A
Urban	1.296	0.743	1.138
Humid Rural	2.006	N/A	N/A
Humid Urban	1.235	N/A	N/A

Data from rural scenes also indicate a clear difference between MWIR and LWIR  $\sigma_T$  at different times of day. In almost all daytime images analyzed, MWIR has a higher scene contrast than LWIR due to the additional solar reflections in the MWIR that contributed to the SCT and  $\sigma_T$ . The ratio in MWIR/LWIR during the day averaged over all scenes is 1.224. The day  $\sigma_T$  ranged from 2K to 6.5K in the MWIR and 1K to 6.5K in the LWIR. The night  $\sigma_T$  was significantly lower than day  $\sigma_T$ . At night, the LWIR  $\sigma_T$  was almost always larger than the MWIR  $\sigma_T$ ; the average ratio was 0.729. The night  $\sigma_T$  ranged from 0.4K to 1.5K in the MWIR and 0.6K to 2K in the LWIR.

In the urban environment, there were many man-made materials and structures that had even more emissivity and reflectivity variations than rural scene objects. The data was spread more in the urban environment than the rural data, as expected. However, the overall trends were the same; there is no significant jump in the average figure of merit from rural to urban at daytime or nighttime. Day  $\sigma_T$  favored the MWIR slightly and night  $\sigma_T$  favored the LWIR. The night MWIR  $\sigma_T$  was generally slightly lower than LWIR  $\sigma_T$  by roughly the same ratio seen in the urban environment. The day  $\sigma_T$  ranges were about the same as the urban  $\sigma_T$  and the night  $\sigma_T$  were higher than rural day  $\sigma_T$ . One reason for this was the hot objects associated with buildings and infrastructure as well as windows that reflected the cold sky. One interesting note was that when the day measurements were made with cloud cover, the LWIR and MWIR  $\sigma_T$  were much closer, suggesting that the reflectivities that allowed the cold sky to contribute were then reflecting clouds that were at the same equivalent blackbody temperatures in the MWIR and LWIR. The cloud-covered day  $\sigma_T$  were not as cold as the night, but not as high as sunny day  $\sigma_T$ .

In a humid environment, there was a change in both the atmosphere and the type of foliage that is native to the area. There were much more green trees and vegetation in the data collection point in Orlando, FL than in Tucson, AZ. The ratio of MWIR to LWIR  $\sigma_T$  is roughly the same in a humid

urban environment as it is in a dry urban environment. This is because the content of the scene is essentially the same since there is no significant amount of green foliage as compared to the dry urban scenes. To study the effects of a humid atmosphere on  $\sigma_T$  and SCT, this study should be repeated over longer ranges such that the atmosphere has a more significant effect on measured radiance. The ratio of MWIR to LWIR  $\sigma_T$  is much higher in a rural humid environment than a dry humid environment. It is possible that this is due to spectral reflectivity/emissivity properties of the foliage materials being more varied in the MWIR. The data collected, however, is not enough to provide concrete conclusions and this study should be repeated over multiple days to verify any findings.

During heavy amounts of precipitation,  $\sigma_T$  was reduced in both MWIR and LWIR. Rainwater cooled everything in the scene to about the same temperature, meaning all radiance variation was due to variations in emissivity.  $\sigma_T$  was far lower in both bands, however during the daytime there was some diffuse sunlight which was reflected in MWIR but not LWIR. The ratio of MWIR to LWIR  $\sigma_T$  during rain/daytime starts between 1 and 1.5 and moves below 1 as the rain continues and the day fades. Interestingly, when the rain stops at nighttime, a spike is seen in LWIR  $\sigma_T$  but not MWIR  $\sigma_T$ . During the days after rainfall, the cycle eventually returned to normal with greater  $\sigma_T$  in MWIR at day and greater  $\sigma_T$  in LWIR at night. This data indicates possible trends in emissive band SCT during rainfall, but more data should be collected before any concrete conclusions are drawn.

For pilotage and scene-based navigation at night, the LWIR has more contrast, so LWIR would generally be preferred. Depending on the type of detector used, the LWIR provides roughly 15 times the power scene contrast of the MWIR and the LWIR provides roughly 30 times the photon counting contrast of the MWIR. However, depending on the type of sensor used and its noise

properties, this difference in SCT between MWIR and LWIR at night may be inconsequential for pilotage performance. For a sensor with a high NETD, TTP drops off at a much higher SCT than a sensor with a low NETD. Figure 6.1 illustrates this point using the precipitation data (this data has the widest range of  $\sigma_T$ ), TTP is calculated as a function of SCT (SCT is assumed to be equal to  $3\sigma_T$  for the purposes of these calculations) for a low NETD MWIR sensor and a low NETD LWIR sensor. Figure 6.2 shows the same data on a shortened y-axis scale.

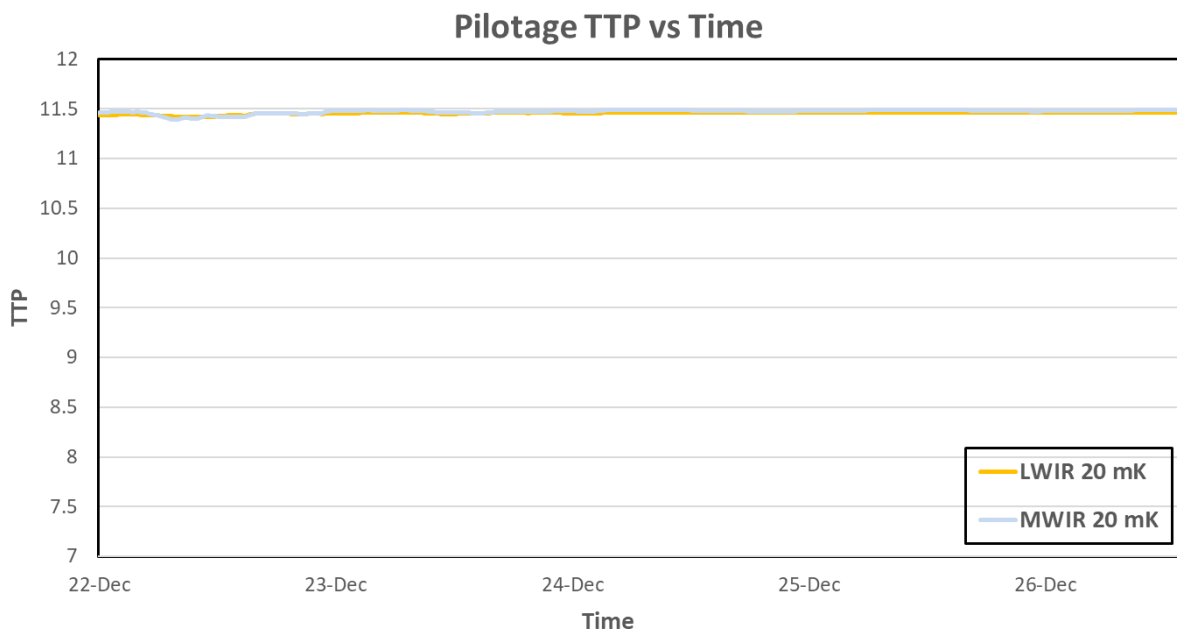


Figure 6.1: Low NETD Pilotage Sensor TTP vs time over multiple days (using precipitation data) for LWIR/MWIR

Even at extremely low SCT due to precipitation, the performance of a low-NETD sensor is not affected in a pilotage application. Figure 6.2 depicts the performance of a medium NETD sensor in the same conditions.

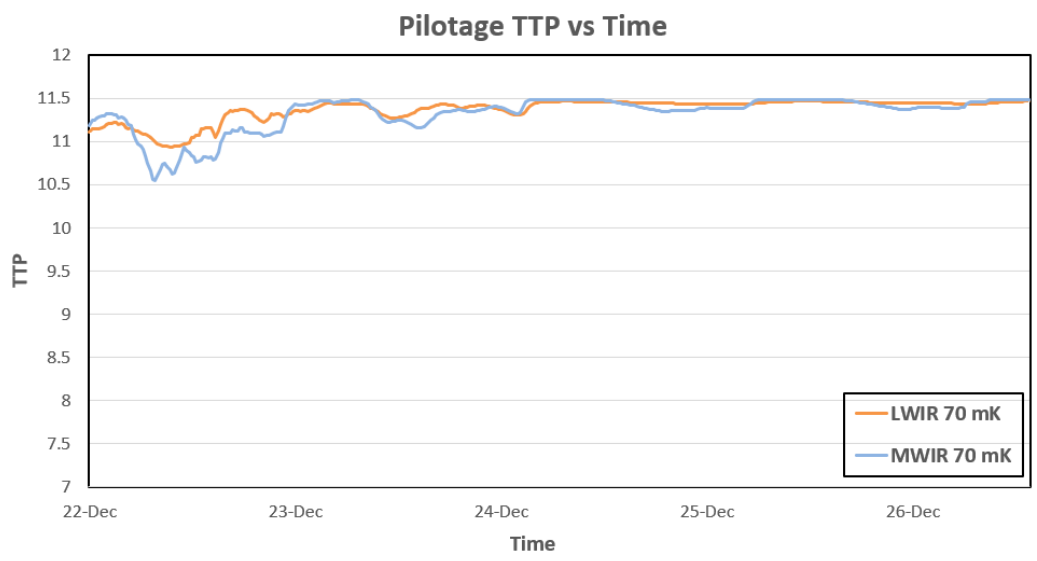


Figure 6.2 : Medium NETD Pilotage Sensor TTP vs time over multiple days (using precipitation data) for LWIR/MWIR

For a medium NETD sensor, pilotage performance is hindered during times of low SCT, but still has usable performance. Figure 6.3 depicts the performance of a high NETD sensor in the same conditions.

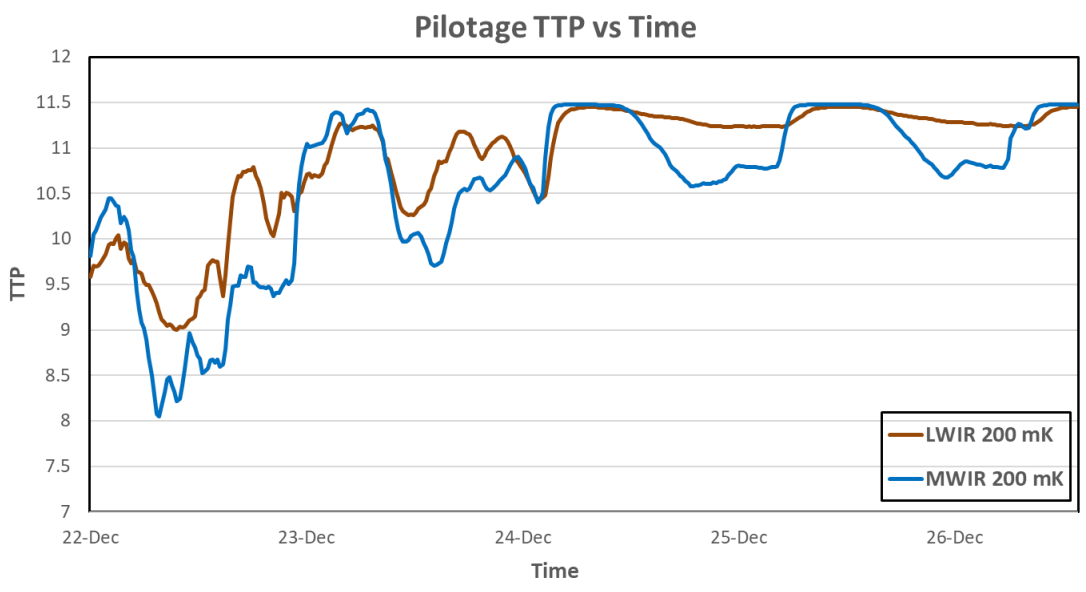


Figure 6.3: High NETD Pilotage Sensor TTP vs time over multiple days (using precipitation data) for LWIR/MWIR



For the high NETD sensor, performance of a pilotage system is hindered by a lot during times of extreme low SCT (precipitation). Additionally, there is some degradation during a normal nighttime with this large amount of noise. If SCT does become a factor during nighttime or periods of low SCT, LWIR is preferred over MWIR due to increased SCT at night. The performance of the LWIR sensor in this chart is nearly always better than the performance of the MWIR sensor due to the increased SCT during periods of low SCT.

The data and analysis results show that the scene clutter is much lower during the night, so search and detection with hot vehicles and humans at night is much easier than the same task during the day in both the MWIR and LWIR bands. Also, at night, clutter is smaller in the MWIR so searching for vehicles or humans at night would be easier in the MWIR, especially in the rural environment. During the day, clutter is smaller in the LWIR so searching for vehicles or humans would be easier with a LWIR sensor.

In future work, SCT should further be studied in rainy and humid conditions, especially at longer ranges. Additionally, most of the time an imager is not looking only at objects on the ground; there is some amount of cold sky contained in an image for many applications. Ground contrast should also be studied when using dynamic range compression techniques for cold sky and it should be determined whether the colder sky in LWIR leads to decreased ground contrast.

## Chapter 7 Conclusions

The data and analysis presented suggest that MWIR has higher  $\sigma_T$  and SCT than LWIR in the daytime with sunny conditions. They are about the same in cloud covered conditions. At night, MWIR has less  $\sigma_T$  and SCT than LWIR by a rough factor of 2/3rds. Humidity in the atmosphere does not have a significant effect on SCT, but changes in foliage due to humidity may boost MWIR SCT. Rain significantly degrades SCT in both emissive bands; SCT is near equal between bands during rain at daytime.

For pilotage and scene-based navigation in environments with low scene contrast, especially for sensors with high noise, slight improvements in scene contrast matter more than ever, meaning LWIR may be a safer choice. While the night differences in SCT are not significant (roughly 2/3rds), there may be other reasons to consider MWIR systems especially if the noise in the sensors used is low.

For a targeting system, apparent target contrast is greater in LWIR at daytime and greater in MWIR at nighttime. Benefits from increased target contrast may not outweigh other benefits ascribed to choosing a specific band, but these conclusions are worth keeping in mind when designing EO/IR systems.

## REFERENCES

1. U.S Navy, Naval Air Systems Command. *Electronic Warfare and Radar Systems Engineering Handbook*, 1997.
2. "The Electromagnetic Spectrum." *The Electromagnetic Spectrum*, [www.columbia.edu/~vjd1/electromag\\_spectrum.htm](http://www.columbia.edu/~vjd1/electromag_spectrum.htm). Accessed 10 Feb. 2024.
3. Vollmerhausen and Eddie Jacobs, "The Targeting Task Performance (TTP) Metric A New Model for Predicting Target Acquisition Performance," DTIC Technical Report AMSEL-NV-TR-230 Revision 20 April 2004.
4. Vollmerhausen, Richard H., Eddie Jacobs, and Ronald Driggers (2004), "New metric for predicting target acquisition performance," OE, Vol.43, No.11, pp 2806-2818, November 2004.
5. R. Driggers, M. Friedman, J. Devitt, O. Furxhi, A. Singh, Introduction to Infrared and Electro-Optical Systems, Artech House, Third Edition, 2022
6. Ronald G. Driggers, Eddie L. Jacobs, Richard H. Vollmerhausen, Barbara O'Kane, Mid Self, Steve Moyer, Jonathan G. Hixson, Gary Page, Keith Krapels, David Dixon, Regina Kistner, John Mazz, "Current infrared target acquisition approach for military sensor design and wargaming," Proc. SPIE Vol. 6207, 620709, Infrared Imaging Systems: Design, Analysis, Modeling, and Testing XVII; Gerald C. Holst; Ed. May 2006.
7. Vollmerhausen, Richard H., and Trang Bui. "Using a targeting metric to predict the utility of an EO imager as a pilotage aid." *Infrared Imaging Systems: Design, Analysis, Modeling, and Testing XVII*. Vol. 6207. SPIE, 2006.

8. Richard H. Vollmerhausen, "Design criteria for helicopter night pilotage sensors," Proc. SPIE 2075, Passive Sensors, 20750Q (29 January 1992)
9. Yasumasa Itakura, Suteo Tsutsumi, Tohru Takagi, "Statistical properties of the background noise for the atmospheric windows in the intermediate infrared region," Infrared Physics, Volume 14, Issue 1, 1974, Pages 17-29, ISSN 0020-0891.
10. M. C. Hetzler, R. M. Smith, R. C. DuVarney, J. M. Marks, "A Study Of Clutter In Infrared Backgrounds," Proc. SPIE 0781, Infrared Image Processing and Enhancement, (16 September 1987); <https://doi.org/10.1117/12.940527>
11. Marshall R. Weathersby, David E. Schmieder, "An Experiment Quantifying The Effect Of Clutter On Target Detection," Proc. SPIE 0510, Infrared Technology X, (21 January 1985); <https://doi.org/10.1117/12.945002>
12. Jonathan G. Hixson, Brian Teaney, Eddie L. Jacobs, "Modeling the effects of image contrast on thermal target acquisition performance," Proc. SPIE 6207, Infrared Imaging Systems: Design, Analysis, Modeling, and Testing XVII, 62070H (15 May 2006);
13. R. Driggers, M. Friedman, J. Devitt, O. Fuxhi, A. Singh, Introduction to Infrared and Electro-Optical Systems, Artech House, Third Edition, 2022, page 169.
14. Shane Jordan, Ronald Driggers, Orges Fuxhi, Patrick Leslie, Col Cavanaugh, Kyle Renshaw, Eddie Jacobs, "Comparison of scene contrast temperature in mid-wave infrared and long-wave infrared," Opt. Eng. 62(11) 113107 (27 November 2023)